



Dynamic Plasticity and Fracture in High Density Polycrystals: Constitutive Modeling and Numerical Simulation

by J. D. Clayton

ARL-RP-151

September 2006

**A reprint from the *Journal of Mechanics and Physics of Solids*,
vol. 53, pp. 261–301, 2005.**

NOTICES

Disclaimers

The findings in this report are not to be construed as an official Department of the Army position unless so designated by other authorized documents.

Citation of manufacturer's or trade names does not constitute an official endorsement or approval of the use thereof.

Destroy this report when it is no longer needed. Do not return it to the originator.

Army Research Laboratory

Aberdeen Proving Ground, MD 21005-5066

ARL-RP-151**September 2006**

Dynamic Plasticity and Fracture in High Density Polycrystals: Constitutive Modeling and Numerical Simulation

J. D. Clayton

Weapons and Materials Research Directorate, ARL

A reprint from the *Journal of Mechanics and Physics of Solids*,
vol. 53, pp. 261–301, 2005.

REPORT DOCUMENTATION PAGE				Form Approved OMB No. 0704-0188	
Public reporting burden for this collection of information is estimated to average 1 hour per response, including the time for reviewing instructions, searching existing data sources, gathering and maintaining the data needed, and completing and reviewing the collection information. Send comments regarding this burden estimate or any other aspect of this collection of information, including suggestions for reducing the burden, to Department of Defense, Washington Headquarters Services, Directorate for Information Operations and Reports (0704-0188), 1215 Jefferson Davis Highway, Suite 1204, Arlington, VA 22202-4302. Respondents should be aware that notwithstanding any other provision of law, no person shall be subject to any penalty for failing to comply with a collection of information if it does not display a currently valid OMB control number. PLEASE DO NOT RETURN YOUR FORM TO THE ABOVE ADDRESS.					
1. REPORT DATE (DD-MM-YYYY) September 2006		2. REPORT TYPE Reprint		3. DATES COVERED (From - To) 2003–2006	
4. TITLE AND SUBTITLE Dynamic Plasticity and Fracture in High Density Polycrystals: Constitutive Modeling and Numerical Simulation				5a. CONTRACT NUMBER	
				5b. GRANT NUMBER	
				5c. PROGRAM ELEMENT NUMBER	
6. AUTHOR(S) J. D. Clayton				5d. PROJECT NUMBER WHPR01B	
				5e. TASK NUMBER	
				5f. WORK UNIT NUMBER	
7. PERFORMING ORGANIZATION NAME(S) AND ADDRESS(ES) U.S. Army Research Laboratory ATTN: AMSRD-ARL-WM-TD Aberdeen Proving Ground, MD 21005-5066				8. PERFORMING ORGANIZATION REPORT NUMBER ARL-RP-151	
9. SPONSORING/MONITORING AGENCY NAME(S) AND ADDRESS(ES)				10. SPONSOR/MONITOR'S ACRONYM(S)	
				11. SPONSOR/MONITOR'S REPORT NUMBER(S)	
12. DISTRIBUTION/AVAILABILITY STATEMENT Approved for public release; distribution is unlimited.					
13. SUPPLEMENTARY NOTES A reprint from the <i>Journal of Mechanics and Physics of Solids</i> , vol. 53, pp. 261–301, 2005.					
14. ABSTRACT Presented is a constitutive framework for modeling the dynamic response of polycrystalline microstructures, posed in a thermodynamically consistent manner and accounting for finite deformation, strain rate dependence of flow stress, thermal softening, thermal expansion, heat conduction, and thermoelastic coupling. Assumptions of linear and square-root dependencies, respectively, of the stored energy and flow stresses upon the total dislocation density enable calculation of the time-dependent fraction of plastic work converted to heat energy. Fracture at grain boundary interfaces is represented explicitly by cohesive zone models. Dynamic finite element simulations demonstrate the influences of interfacial separation, random crystallographic orientation, and grain morphology on the high-rate tensile response of a realistic two-phase material system consisting of comparatively brittle pure tungsten (W) grains embedded in a more ductile matrix of tungsten–nickel iron (W–Ni–Fe) alloy. Aspects associated with constitutive modeling of damage and failure in the homogenized material system are discussed in light of the computational results.					
15. SUBJECT TERMS microcracking, microstructures, crystal plasticity, finite elements					
16. SECURITY CLASSIFICATION OF:			17. LIMITATION OF ABSTRACT UL	18. NUMBER OF PAGES 48	19a. NAME OF RESPONSIBLE PERSON John D. Clayton
a. REPORT UNCLASSIFIED	b. ABSTRACT UNCLASSIFIED	c. THIS PAGE UNCLASSIFIED			19b. TELEPHONE NUMBER (Include area code) 410-306-0975



Dynamic plasticity and fracture in high density polycrystals: constitutive modeling and numerical simulation

J.D. Clayton*

U.S. Army Research Laboratory, Impact Physics Branch, Aberdeen Proving Ground, MD 21005-5069, USA

Received 22 April 2004; received in revised form 16 June 2004; accepted 18 June 2004

Abstract

Presented is a constitutive framework for modeling the dynamic response of polycrystalline microstructures, posed in a thermodynamically consistent manner and accounting for finite deformation, strain rate dependence of flow stress, thermal softening, thermal expansion, heat conduction, and thermoelastic coupling. Assumptions of linear and square-root dependencies, respectively, of the stored energy and flow stresses upon the total dislocation density enable calculation of the time-dependent fraction of plastic work converted to heat energy. Fracture at grain boundary interfaces is represented explicitly by cohesive zone models. Dynamic finite element simulations demonstrate the influences of interfacial separation, random crystallographic orientation, and grain morphology on the high-rate tensile response of a realistic two-phase material system consisting of comparatively brittle pure tungsten (W) grains embedded in a more ductile matrix of tungsten–nickel iron (W–Ni–Fe) alloy. Aspects associated with constitutive modeling of damage and failure in the homogenized material system are discussed in light of the computational results.

Published by Elsevier Ltd.

Keywords: A. Microcracking; A. Microstructures; B. Crystal plasticity; C. Finite elements

*Tel.: +1-410-306-0975; fax: +1-410-306-0783.

E-mail address: jclayton@arl.army.mil (J.D. Clayton).

1. Introduction

Tungsten heavy alloys (WHAs) are attractive candidates for use as kinetic energy penetrators (i.e., armor-piercing projectiles) because of their relatively large mass density, high melting point, and high strength at elevated rates of loading (Cai et al., 1995). Previous experimental and numerical investigations reported in the literature (Weerasooriya and Beaulieu, 1993; Ramesh, 1994; Subhash et al., 1994a, b; Zhou et al., 1994; Zhou and Clifton, 1997; Weerasooriya, 1998, 2003; O'Donnell and Woodward, 2000; Woodward and O'Donnell, 2000) reveal a variety of failure modes exhibited by WHAs strained at moderate to high rates, including brittle fracture at W–W grain boundaries, matrix-grain decohesion, ductile matrix rupture, transgranular cleavage of W grains, and adiabatic shear banding. Spallation (material separation due to tensile wave propagation) has been observed in plane shock wave experiments on this material (Dandekar and Weisgerber, 1999). Macroscopic constitutive models (Stevens and Batra, 1998; Wei et al., 2001; Yadav et al., 2001) typically used to represent the two-phase system in numerical simulations currently lack a rigorous description of the kinematics of anisotropic plasticity (e.g. plastic spin), the role of crystallographic orientation of constituent grains, and the effects of crystal morphology on failure processes. Microstructural characteristics such as grain shape, spatial arrangement of grains, and local crystallographic orientation are known to influence the response of the material to thermomechanical loading. Experimental (Bruchey et al., 1991, 1992; Kingman, 1997) and numerical (Schoenfeld and Benson, 1997) methods have demonstrated a possible correlation between lattice orientation of W single crystals and the performance of such crystals as kinetic energy penetrators. Wei et al. (2000) studied the influence of pre-twisting of polycrystalline WHA specimens on the response under combined compressive-shear loading and found that a certain degree of pre-twisting of the microstructure promotes adiabatic shear localization at high strain rates. Such shear localization is considered desirable in armor penetration events, since it is thought to promote a “self-sharpening” effect leading to greater depth of penetration (Magness, 1994; Yadav et al., 2001).

The particular material studied here consists of relatively stiff and brittle pure tungsten grains (BCC), most often nearly equi-axed in shape, embedded in a relatively compliant and ductile matrix (FCC) consisting of nickel (50 wt.%), iron (25 wt.%), and tungsten (25 wt.%). Nominally, the composite microstructure consists of 90% pure W and 10% matrix alloy, leading to an overall weight distribution of 93W-5Ni-2Fe. Fabrication of the composite microstructure is conducted via isostatic pressing and sintering of a mixture of W, Ni, and Fe powders, followed by annealing to remove absorbed hydrogen and then possible quenching, swaging, and/or pre-twisting to alter the dynamic mechanical properties prior to deformation testing at high strain rates (Weerasooriya, 1998; Wei et al., 2000). Typical grain sizes are 10–30 μm for the W crystals and 200–500 μm for the matrix phase (Zamora et al., 1992; Zhou, 1993), meaning that multiple W crystals are often embedded within each single “grain” of the matrix phase.

Previous computational work by Zhou and co-workers (Zhou et al., 1994; Zhou, 1998a, b) elucidated the role of grain morphology, heat conduction, strain- and strain-rate hardening, and thermal softening on the elastoplastic deformation and shear localization of WHAs at nominally high applied rates of shear and combined pressure-shear loading. While grain and matrix phases were resolved discretely in these calculations, each constituent was treated as an isotropically-hardening, hypoelastoelasto-viscoplastic material, thereby neglecting the possibly significant effects of lattice rotation and anisotropic strain hardening associated with the evolution of crystallographic texture within each phase. Thus the potential exists for development of more descriptive constitutive models accounting for local crystallographic orientation effects, models which would simultaneously engender more accuracy to ballistic simulations and support the design of WHA microstructures tailored for enhanced thermomechanical properties. Recent high rate experiments of Weerasooriya (2003) indicated that tensile failure of WHA specimens often initiates via local fracture at W–W (i.e., grain–grain) interfaces, and less often at interfaces between W grains and the matrix phase. Considering W–Ni–Fe alloys of various compositions deformed quasi-statically and at room temperature, Woodward and O'Donnell (2000) ranked contributions of various mechanisms to total crack area, in order of percentage of potential area cracked, as follows in order of descending frequency: W–W interfacial failure, W-matrix interfacial separation, matrix rupture, and cleavage fracture within W grains. However, in a companion publication, O'Donnell and Woodward (2000) emphasized that at higher ambient temperatures (> 373 K), the propensity for cleavage fracture within grains tends to increase at the expense of interfacial fracture. Zamora et al. (1992) observed that microscopic fracture mechanisms and macroscopic fracture toughness measurements vary with chemical composition, grain size, and grain contiguity. Failure strengths of interfaces within the composite microstructure also depend strongly upon processing conditions; for example, slow cooling rates following post-sintering annealing may result in segregation of strength-reducing impurities at interfaces (German et al., 1984). In our numerical framework, we model interface fracture by invoking the cohesive zone approach (Barenblatt, 1959; Dugdale, 1960; Needleman, 1987; Xu and Needleman, 1994; Camacho and Ortiz, 1996). Thus, unlike prior computational investigations that did not consider fracture explicitly, we are able to capture a failure mode that may dominate the response of the WHA material system when subjected to a net tensile hydrostatic stress.

The present work employs single crystalline plasticity models for each phase, as discussed in Section 2. Models for both materials are embedded within a general thermodynamic framework applicable for describing any thermoelastoelasto-viscoplastically-deforming single crystal. Finite deformation, strain-rate dependence, heat conduction, thermal expansion, thermal softening, and thermoelastoelasto coupling are included in the description. Furthermore, our framework enables prediction of the fraction of plastic work stored in the material as residual elastic energy associated with lattice defects (i.e., dislocations). Our treatment of this “stored energy of cold work” can be viewed as an extension to finite crystal plasticity theory of the macroscopic, linearized elastic–plastic framework of Rosakis et al. (2000), who

demonstrated the strain and strain-rate dependence of the fraction of plastic work converted to stored energy.

Cohesive fracture modeling is discussed briefly in Section 3. A temperature- and rate-independent, linear-softening, 2D cohesive finite element approach similar to that of Camacho and Ortiz (1996) is employed here, with new fracture surfaces generated at interfaces between continuum elements when the traction on the interface exceeds the intrinsic fracture strength of the interface (a material parameter). In our computational modeling scheme, fracture surfaces are only generated at interfaces between grains of the same and/or different phases; i.e., intragranular fractures (cleavage of W-grains and matrix rupture) are not included in the cohesive zone description invoked in the present work.

Two-dimensional finite element simulations of deforming, realistic WHA microstructures are conducted, with results given in Section 4. We investigate parametrically the effects of varying the ratio of fracture strengths of W–W interfaces and W–matrix interfaces, the initial lattice orientations of the constituent W crystals and matrix phase, and the representation of the microstructural morphology, the latter obtained from an optical image of a test sample of the actual material. Each of these aspects is shown to influence, to a varying degree, the average stress–strain response and failure behavior of the aggregate. Finally, multiscale issues important in the construction of a macroscopic damage and failure model for the homogenized material system are mentioned, following the framework of Clayton and McDowell (2003, 2004). These issues include description of the contribution of damage entities (i.e., fracture surfaces) to the average deformation gradient for a representative volume of material and the appropriate choice of internal state variables capturing the evolution of damage and its effect upon the average stress supported by representative volume of material.

2. Crystal plasticity formulation

2.1. Kinematics

Let $\mathbf{x} = \mathbf{x}(\mathbf{X}, t)$ represent a smooth time-dependent motion. A multiplicative decomposition of the deformation gradient is assumed:

$$\mathbf{f} \equiv \frac{\partial \mathbf{x}}{\partial \mathbf{X}} = \mathbf{f}^e \mathbf{f}^\theta \mathbf{f}^p, \quad (1)$$

where \mathbf{f}^e , \mathbf{f}^θ , and \mathbf{f}^p represent the kinematics of elasticity and rigid-body rotation, thermal expansion or contraction, and the cumulative contribution of moving crystal defects, respectively. In Eq. (1) and henceforward, juxtaposition implies summation over one set of adjacent indices, i.e., $(\mathbf{AB})_{,k}^i = A_{,j}^i B_{,k}^j$ for arbitrary second-rank tensors \mathbf{A} and \mathbf{B} . In general, none of \mathbf{f}^e , \mathbf{f}^θ , and \mathbf{f}^p is a compatible (i.e., integrable) deformation gradient when considered individually. As shown in Fig. 1, the elastic and thermal terms dictate the deformation of the slip direction contravariant vectors

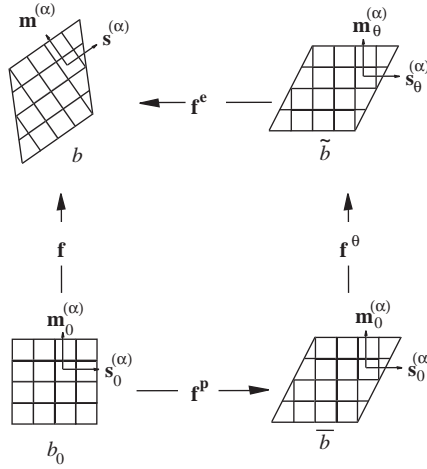


Fig. 1. Deformations, configurations, and slip vectors.

$\mathbf{s}^{(\alpha)}$ and slip plane normal covariant vectors $\mathbf{m}^{(\alpha)}$:

$$\mathbf{s}^{(\alpha)} = \mathbf{f}^e \mathbf{f}^\theta \mathbf{s}_0^{(\alpha)}, \quad \mathbf{m}^{(\alpha)} = \mathbf{m}_0^{(\alpha)} \mathbf{f}^{\theta-1} \mathbf{f}^{e-1}, \quad (2)$$

with the superposed “−1” denoting the inverse operation. The velocity gradient \mathbf{l} referred to the current configuration is written as

$$\mathbf{l} \equiv \frac{\partial \dot{\mathbf{x}}}{\partial \mathbf{x}} = \dot{\mathbf{f}} \mathbf{f}^{-1} = \underbrace{\dot{\mathbf{f}}^e \mathbf{f}^{e-1}}_{\equiv \mathbf{l}^e} + \underbrace{\dot{\mathbf{f}}^e \mathbf{f}^\theta \mathbf{f}^{\theta-1} \mathbf{f}^{e-1}}_{\equiv \mathbf{l}^\theta} + \underbrace{\dot{\mathbf{f}}^e \mathbf{f}^\theta \dot{\mathbf{f}}^p \mathbf{f}^{p-1} \mathbf{f}^{\theta-1} \mathbf{f}^{e-1}}_{\equiv \mathbf{l}^p}, \quad (3)$$

where the superposed dot represents the material time derivative. The thermal deformation is assumed isotropic (Lee et al., 1997), i.e.,

$$\mathbf{l}^\theta = \dot{\mathbf{f}}^\theta \mathbf{f}^{\theta-1} = \alpha_T \dot{\theta} \mathbf{1}, \quad (4)$$

where θ is the temperature change measured from the reference state and α_T is the thermal expansion coefficient giving the change in length per unit current length per unit increment in θ . The unit tensor is written as $\mathbf{1}$. The plastic velocity gradient in the intermediate configuration \bar{b} of Fig. 1 is defined as (Rice, 1971; Asaro, 1983)

$$\bar{\mathbf{l}}^p \equiv \dot{\mathbf{f}}^p \mathbf{f}^{p-1} = \sum_{\alpha=1}^n \dot{\gamma}^{(\alpha)} \mathbf{s}_0^{(\alpha)} \otimes \mathbf{m}_0^{(\alpha)}, \quad (5)$$

with $\dot{\gamma}^{(\alpha)}$ the plastic shearing rate on slip system α , n the number of potentially active slip systems, and \otimes the tensor product.

2.2. Balance laws

Localized balance laws are prescribed in the current configuration as follows:

$$\dot{\rho} + \rho \operatorname{tr}(\mathbf{l}) = 0, \quad \operatorname{div} \boldsymbol{\sigma} + \rho \mathbf{b} = \rho \ddot{\mathbf{x}}, \quad \boldsymbol{\sigma} = \boldsymbol{\sigma}^T, \quad \rho \dot{e} + \operatorname{div} \mathbf{q} - \operatorname{tr}(\boldsymbol{\sigma} \mathbf{g} \mathbf{l}) = \rho r, \quad (6)$$

with ρ , $\boldsymbol{\sigma}$, \mathbf{b} , e , \mathbf{q} , and r the current mass density, contravariant Cauchy stress tensor, body force vector per unit mass, internal energy per unit mass, heat flux vector per unit current area, and energy source per unit mass, respectively. Here, div denotes divergence with respect to current coordinates, e.g. $\operatorname{div} \mathbf{q} = q_{|a}^a = \partial_a q^a + \gamma_{ab}^a q^b$ with the Christoffel symbols of the linear connection in the spatial coordinate system satisfying $2g_{ad}\gamma_{bc}^d = \partial_c g_{ba} + \partial_b g_{ca} - \partial_a g_{cb}$, where we use the compact notation $\partial_a = \partial/\partial x^a$ and the spatial metric satisfies $g_{ab} = \partial_a \mathbf{x} \cdot \partial_b \mathbf{x}$. The trace operation for a second rank tensor \mathbf{A} is denoted by $\operatorname{tr}(\mathbf{A}) = A_{.k}^k$. The local entropy inequality is written as follows, with $\dot{\eta}$ the time rate of entropy production per unit mass:

$$\rho \dot{\eta} \geq -\operatorname{div} \left(\frac{\mathbf{q}}{\theta} \right) + \frac{\rho r}{\theta}. \quad (7)$$

The Helmholtz free energy per unit mass ψ is also introduced:

$$\psi \equiv e - \theta \eta, \quad (8)$$

from which, upon substitution of Eqs. (6) and (8) into Eq. (7), the entropy inequality becomes

$$\operatorname{tr}(\boldsymbol{\sigma} \mathbf{g} \mathbf{l}) - \left(\frac{\mathbf{q} \cdot \nabla_{\mathbf{x}} \theta}{\theta} \right) \geq \rho(\dot{\psi} + \dot{\theta} \eta), \quad (9)$$

with $\nabla_{\mathbf{x}}$ the covariant derivative with respect to \mathbf{x} and \cdot a scalar product operation for vectors, i.e., $\mathbf{a} \cdot \mathbf{b} = a^i g_{ij} b^j$.

2.3. Thermodynamic framework

We assume a Helmholtz free energy potential of the form

$$\psi = \psi(\mathbf{e}^e, \theta, \xi), \quad (10)$$

where the intermediate configuration elastic strain $2(e^e)_{\alpha\beta} = f_{. \alpha}^{ea} g_{ab} f_{. \beta}^{eb} - \tilde{g}_{\alpha\beta}$, with $\tilde{g}_{\alpha\beta}$ a metric tensor on \tilde{b} , which in practice is chosen as Kronecker's delta $\delta_{\alpha\beta}$ for simplicity (Simo and Ortiz, 1985), a typical assumption in finite elastoplasticity (Clayton et al., 2004). The symbol ξ denotes a dimensionless scalar internal variable representing stored micro-elastic energy associated with crystal defects that may impede shearing on each slip system. Expanding the time rate of ψ and inserting the result into inequality (9) yields

$$\operatorname{tr}(\boldsymbol{\sigma} \mathbf{g}(\mathbf{l}^e + \mathbf{l}^\theta + \mathbf{l}^\psi)) - \left(\frac{\mathbf{q} \cdot \nabla_{\mathbf{x}} \theta}{\theta} \right) \geq \rho(\partial_{\mathbf{e}^e} \psi : \dot{\mathbf{e}}^e + (\partial_\theta \psi) \dot{\theta} + (\partial_\xi \psi) \dot{\xi} + \dot{\theta} \eta), \quad (11)$$

where the scalar product of two second rank objects is defined by $\mathbf{A} : \mathbf{B} = A^{ij} B_{ij}$, and where the subscript following the ∂ -operator denotes partial differentiation with respect to the subscripted variable. Additional algebraic manipulations give

$$\begin{aligned} \frac{\rho}{\tilde{\rho}} (\mathbf{s}^e - \tilde{\rho} \partial_{\mathbf{e}^e} \psi) : \dot{\mathbf{e}}^e + (tr(\boldsymbol{\sigma} \mathbf{g}) \alpha_T - \rho(\partial_\theta \psi) - \rho \eta) \dot{\theta} - \rho(\partial_\xi \psi) \dot{\xi} \\ + \sum_{\alpha=1}^n \tau^{(z)} \dot{\gamma}^{(z)} \geq \left(\frac{\mathbf{q} \cdot \nabla_{\mathbf{x}} \theta}{\theta} \right), \end{aligned} \quad (12)$$

where $\tilde{\rho}$ is the mass density in configuration \tilde{b} and the elastic second Piola–Kirchhoff stress $(s^e)^{\alpha\beta} \equiv j^e f_{.a}^{e-1\alpha} \sigma^{ab} f_{.b}^{e-1\beta}$ with $j^e \equiv \det \mathbf{f}^e \sqrt{\det \mathbf{g} / \det \tilde{\mathbf{g}}} = \tilde{\rho} / \rho$ (Teodosiu, 1967). The resolved Cauchy stress for slip system α is defined by $\tau^{(z)} \equiv: \boldsymbol{\sigma}(\mathbf{g} \mathbf{s}^{(z)} \otimes \mathbf{m}^{(z)})$. Assuming that the independent variables in the potential (10) can be varied individually (Coleman and Noll, 1963; Scheidler and Wright, 2001), we then have

$$\mathbf{s}^e = \tilde{\rho} \partial_{\mathbf{e}^e} \psi, \quad (13)$$

$$\eta = \underbrace{\frac{\alpha_T}{\rho} tr(\boldsymbol{\sigma} \mathbf{g}) - \partial_\theta \psi}_{\equiv \chi}, \quad (14)$$

$$\sum_{\alpha=1}^n \tau^{(z)} \dot{\gamma}^{(z)} - \rho(\partial_\xi \psi) \dot{\xi} \geq \left(\frac{\mathbf{q} \cdot \nabla_{\mathbf{x}} \theta}{\theta} \right). \quad (15)$$

Notice that the first term on the right of Eq. (14), denoted by χ , arises as a consequence of the explicit inclusion of thermal expansion/contraction in the kinematic description (1). Rearranging the energy balance in Eq. (6) by appealing to Eqs. (13) and (14) leads to

$$\rho \theta \dot{\chi} - \rho \theta \partial_\theta \dot{\psi} = \rho r - \text{div } \mathbf{q} + \sum_{\alpha=1}^n \tau^{(z)} \dot{\gamma}^{(z)} - \rho(\partial_\xi \psi) \dot{\xi}. \quad (16)$$

By defining the specific heat capacity \hat{c} as

$$\hat{c} \equiv \partial_\theta e = \partial_\eta e(\partial_\theta \eta) = -\theta(\partial_{\theta\theta} \psi) + \partial_\eta e \partial_\theta \chi, \quad (17)$$

where we have invoked the differential of relation (8), and by assuming isotropic heat conduction in the current configuration dictated by Fourier's law (Zhou et al., 1994):

$$\mathbf{q} = -k \nabla_{\mathbf{x}} \theta, \quad (18)$$

with $k(\mathbf{x})$ the thermal conductivity, we can rewrite the localized energy balance (16) as

$$\underbrace{\rho \hat{c} \dot{\theta}}_{\text{temperature change}} = \underbrace{\sum_{\alpha=1}^n \tau^{(\alpha)} \dot{\gamma}^{(\alpha)}}_{\text{plastic dissipation}} - \underbrace{\rho((\partial_{\xi} \psi) - \theta(\partial_{\theta} \xi \psi)) \dot{\xi}}_{\text{energy of lattice defects}} + \underbrace{\rho \theta \partial_{\theta \mathbf{e}^e} \psi : \dot{\mathbf{e}}^e}_{\text{thermoelastic coupling}} + \underbrace{\text{div}(k \nabla_{\mathbf{x}} \theta)}_{\text{heat conduction}} + \underbrace{\rho r}_{\text{heat supply}}. \quad (19)$$

2.4. Constitutive models

A free energy potential per unit intermediate configuration volume is specified as

$$\tilde{\rho} \psi = \frac{1}{2} \mathbf{e}^e : \mathbf{c}(\theta, \xi) : \mathbf{e}^e + \frac{1}{2} \kappa \mu(\theta, \xi) \xi^2 + \gamma(\theta), \quad (20)$$

where \mathbf{c} and μ are the elastic modulus tensor in configuration \tilde{b} and an effective shear modulus, respectively, and κ is a dimensionless, material-dependent scalar parameter that we assume is independent of strain rate and temperature. The function $\gamma(\theta) = -\hat{c} \theta \ln(\theta/\theta_0)$ accounts for the purely thermal energy (Rosakis et al., 2000), with θ_0 a reference temperature at which $\gamma = 0$. We shall later demonstrate the explicit relationship between κ and the fraction of plastic dissipation converted to heat energy (Eq. (36)) and will use this relationship to select appropriate values of κ . From Eq. (13) and partial differentiation of Eq. (20), we see that the stress satisfies the linear-hyperelastic relationship $\mathbf{s}^e = \mathbf{c} : \mathbf{e}^e$, or $(s^e)^{\alpha\beta} = c^{\alpha\beta\gamma\delta} (e^e)_{\gamma\delta}$, an adequate description for the relatively small elastic strains that emerge in the simulations conducted in the present study. Note that, should the model be used in future work for simulation of impact events that may engender shockwaves and large volumetric strains in the material, we suggest an augmentation of our description, for example with an equation-of-state type formulation (cf. Grüneisen, 1926), to address possibly nonlinear relationships between pressure, mass density, and temperature.

A power-law viscoplastic flow rule (Hutchinson, 1976) is chosen to model the time rate of plastic deformation in each phase:

$$\dot{\gamma}^{(\alpha)} = \dot{\gamma}_0 \left(\frac{\tilde{\tau}^{(\alpha)}}{g^{(\alpha)}} \right)^m \text{sgn}(\tilde{\tau}^{(\alpha)}). \quad (21)$$

Here $\dot{\gamma}_0$ and m are material parameters, $g^{(\alpha)}$ is the slip resistance due to dislocation barriers, $\tilde{\tau}^{(\alpha)} \equiv j^e \tau^{(\alpha)}$ is the projected shear stress pulled back to the intermediate configuration \tilde{b} , and $\text{sgn}(x) = x/|x|$, with $\text{sgn}(0) = 1$. Thermal softening attributed to increased dislocation mobility at high temperatures is incorporated via the power-law form (Klopp et al., 1985)

$$g^{(\alpha)} = g_0^{(\alpha)} (\theta/\theta_0)^p, \quad (22)$$

with $g_0^{(z)}$ the flow resistance at reference temperature θ_0 (a material parameter) and p a dimensionless constant for each material. We postulate the following relationship between the “average” hardening on each system at fixed reference temperature and the internal variable ξ :

$$\frac{1}{n} \sum_{\alpha=1}^n (g_0^{(z)} - g_y^{(z)}) = \hat{\alpha} \mu(\theta_0, 0) \underbrace{b\sqrt{\rho_T}}_{\equiv \xi}, \quad (23)$$

with $g_y^{(z)}$ an initial yield stress, b the magnitude of the Burgers vector, and ρ_T the total dislocation line length per unit intermediate configuration volume associated with shearing impedance. The square-root dependence of flow stress on dislocation density is a common assumption in the plasticity and materials science literature (Taylor, 1934; Kuhlmann-Wilsdorf, 1985, 1989; Zikry and Kao, 1996; Kameda and Zikry, 1998; Ashmawi and Zikry, 2003), as is the assumption of linear dependence of stored lattice energy on dislocation density (Bammann, 2001; Regueiro et al., 2002; Svendsen, 2002) implied jointly by Eqs. (20) and (23). The scalar proportionality factor $\hat{\alpha}$ accounts for dislocation interactions (Kobytev et al., 1984; Ashmawi and Zikry, 2003). Both lattice friction stress and effects of the initial dislocation density are incorporated in $g_y^{(z)}$, the former deemed important in characterizing the flow stress of BCC metals such as tungsten (Qiu et al., 2001), the latter implying that ρ_T is a measure of the change in total dislocation density relative to the initial state.

We now focus attention upon pure W crystals, for which we permit slip in the $\{111\}$ close-packed directions on any of the $\{110\}$ and $\{112\}$ families of planes, resulting in the number of potentially active slip systems $n = 24$ (Subhash et al., 1994a). Possible slip on $\{123\}$ planes, typically inactive at room temperature (Argon and Maloof, 1966; Subhash et al., 1994a), is not represented in our model. Because single crystalline W is very nearly elastically isotropic, we have, with the dependencies of elastic moduli on internal structure ξ suppressed henceforth for simplicity:

$$c^{\alpha\beta\chi\delta} = \lambda(\theta) \tilde{g}^{\alpha\beta} \tilde{g}^{\chi\delta} + \mu(\theta) (\tilde{g}^{\alpha\chi} \tilde{g}^{\beta\delta} + \tilde{g}^{\alpha\delta} \tilde{g}^{\beta\chi}), \quad (24)$$

with Lamé’s constant λ and $\tilde{g}^{\alpha\beta}$ contravariant components of the metric tensor on configuration \tilde{b} . Evolution of slip resistance at reference temperature θ_0 is specified by a hardening-minus-dynamic-recovery relation (Armstrong and Frederick, 1966; Horstemeyer et al., 1999):

$$\dot{g}_0^{(\alpha)} = A \sum_{\beta=1}^n q_{\beta}^{\alpha} |\dot{\gamma}^{(\beta)}| - B g_0^{(\alpha)} \sum_{\beta=1}^n |\dot{\gamma}^{(\beta)}|, \quad (25)$$

with the interaction matrix satisfying

$$q_{\beta}^{\alpha} = \delta_{\beta}^{\alpha} + q(1 - \delta_{\beta}^{\alpha}), \quad (26)$$

where q is the latent hardening ratio.

We now discuss the constitutive model for W–Ni–Fe matrix material, for which the number of potentially active slip systems is chosen as $n = 12$. Dislocation glide is assumed to be the dominant plastic deformation mode for this FCC metal, occurring

in $\langle 110 \rangle$ close-packed directions on $\{111\}$ planes. Elastic isotropy is also assumed for this phase (Zhou et al., 1994), meaning that Eq. (24) applies, though with elastic stiffness constants for the matrix substantially lower in magnitude than those for the pure W. Strain rate- and temperature-dependent slip resistances in crystals comprising the matrix phase are also specified via relations (25) and (26), albeit with different values of A , B , and q than those used for the pure W grains.

2.5. Numerical implementation and material parameters

Two idealized sets of thermal boundary conditions are considered now for the purposes of calibrating model parameters: isothermal and adiabatic. Note, however, that heat conduction is fully taken into account in the theoretical framework and in the explicit finite element implementation discussed in later parts of the current work. A fully implicit, hyperelastic-viscoplastic algorithm (Cuitiño and Ortiz, 1992; McGinty, 2001) is employed here to integrate the elastic–plastic constitutive response. Let subscripts t and $t + \Delta t$ denote consecutive computation times in a nonlinear analysis, i.e., start and end times in a particular iteration cycle. The slip rates for a given time increment spanning times t and $t + \Delta t$ are found implicitly, using values of the resolved shear stress and hardening variables at the end of the cycle:

$$\dot{\gamma}^{(z)} = \dot{\gamma}_0 \left| \frac{\tilde{\tau}_{t+\Delta t}^{(z)}}{g_{t+\Delta t}^{(z)}} \right|^m \text{sgn}(\tilde{\tau}_{t+\Delta t}^{(z)}). \quad (27)$$

Since $\tilde{\tau}_{t+\Delta t}^{(z)}$ and $g_{t+\Delta t}^{(z)}$ depend upon the solution variables $\dot{\gamma}^{(z)}$, an iterative procedure is used to solve Eq. (27). Notice that $\tilde{\tau}_{t+\Delta t}^{(z)}$ and $g_{t+\Delta t}^{(z)}$ depend upon θ , through Eq. (22) and the temperature dependence of elastic moduli, Eq. (24). For the isothermal problem, $\dot{\theta} = 0$ and $r = 0$ by assumption, meaning that \mathbf{q} of Eq. (18) varies spatially and temporally such that the energy balance (19) is satisfied throughout the analysis. We also assume $\mathbf{f}_{t \geq 0}^0 = \mathbf{1}$ for the isothermal case.

For the adiabatic problem, we prescribe $\nabla_{\mathbf{x}}\theta = \mathbf{0}$, $r = 0$, and initial conditions $\mathbf{f}_{t=0}^0 = \mathbf{1}$ and $\dot{\theta}_{t=0} = 0$. The temperature rate for a given time increment spanning times t and $t + \Delta t$ is found explicitly using quantities at time t :

$$\dot{\theta} = \left(\frac{\beta}{\rho \hat{c}} \sum_{z=1}^n \tau^{(z)} \dot{\gamma}^{(z)} + \frac{\theta}{\hat{c}} \partial_{\theta}(\mathbf{s}^e : \dot{\mathbf{e}}^e) \right) \Big|_t, \quad (28)$$

where

$$\beta \equiv \left(\sum_{z=1}^n \tau^{(z)} \dot{\gamma}^{(z)} - \rho((\partial_{\xi}\psi) - \theta(\partial_{\theta\xi}\psi))\dot{\xi} \right) \left(\sum_{z=1}^n \tau^{(z)} \dot{\gamma}^{(z)} \right)^{-1}, \quad (29)$$

such that $1 - \beta$ is the ratio of the time rate of stored energy of cold working to the rate of plastic dissipation (Taylor and Quinney, 1934). Note that while β is often assumed in practice to acquire a fixed value for a particular material regardless of the temperature-deformation history, with a value of $0.8 \leq \beta \leq 1.0$ typical for engineering

metals (Kallend and Huang, 1984; Aravas et al., 1990; Zhou et al., 1994), we do not resort to such a constitutive assumption here. We do however make the usual assertion that the specific heat capacity for each material, $\hat{c} = \text{constant}$, a reasonable assumption for pure tungsten over the temperature range encountered in our subsequent calculations (Gray, 1972). The temperature at time $t + \Delta t$ is updated simply via

$$\theta_{t+\Delta t} = \theta_t + \dot{\theta}\Delta t, \quad (30)$$

while the thermal deformation gradient at the end of the step is found as

$$\mathbf{f}_{t+\Delta t}^{\theta} = \exp(\alpha_T \dot{\theta} \mathbf{1} \Delta t) \mathbf{f}_t^{\theta}, \quad (31)$$

with $\exp(\cdot)$ the matrix exponential function. For a given time increment in an adiabatic analysis, Eqs. (27) are solved implicitly using values of $\dot{\theta}$, $\theta_{t+\Delta t}$, and $\mathbf{f}_{t+\Delta t}^{\theta}$ found via (28)–(31). The thermoelastic term in Eq. (19), upon assuming $j^{\theta} \equiv \det \mathbf{f}^{\theta} \approx 1 + 3\alpha_T(\theta - \theta_0)$ can be rewritten as

$$\begin{aligned} \rho \theta \partial_{\theta} \psi : \dot{\mathbf{e}} &= \theta j^{\theta-1} \partial_{\theta}(\mathbf{s}^e : \dot{\mathbf{e}}^e) - \rho \theta j^{\theta} \partial_{\theta}(j^{\theta-1})(\mathbf{s}^e : \dot{\mathbf{e}}^e) \\ &\approx \theta j^{\theta-1} \{ [(\partial_{\theta} \lambda) \tilde{g}^{\alpha\beta} \tilde{g}^{\gamma\delta} + (\partial_{\theta} \mu)(\tilde{g}^{\alpha\gamma} \tilde{g}^{\beta\delta} + \tilde{g}^{\alpha\delta} \tilde{g}^{\beta\gamma})](\dot{e}^e)_{\gamma\delta} \\ &\quad + 3\alpha_T(j^{\theta-1} s^{e\alpha\beta})\}(\dot{e}^e)_{\alpha\beta}. \end{aligned} \quad (32)$$

The dependencies of the elastic moduli of the pure W grains on temperature were obtained (to second order) from the compilation of Yih and Wang (1979):

$$\partial_{\theta} \lambda = -3.4 + 0.0065 T \text{ MPa}/^{\circ}\text{C}, \quad \partial_{\theta} \mu = -10.3 - 0.0041 T \text{ MPa}/^{\circ}\text{C}, \quad (33)$$

where $T \equiv \theta - 273$ is the temperature in degrees C. Thermal dependencies of elastic moduli of the matrix phase were neglected in these computations, due simply to lack of experimental data.

A material point simulator was used to generate average stress–strain and temperature histories for aggregates of one or more grains, in order to calibrate constitutive model parameters. In these deformation-controlled simulations, velocities were prescribed as constant and material accelerations were taken as zero. Also, Taylor’s (1938) assumption was invoked for polycrystalline simulations, meaning that \mathbf{f} was identical for each grain in the aggregate throughout the time history of deformation. For adiabatic analyses, each grain maintained its own temperature, i.e., thermal interactions between crystals were forbidden. Average Cauchy stresses were calculated for the aggregate for each time increment in the analysis via standard volume averaging procedures, assuming each crystal occupied an equal volume in the reference configuration. We emphasize that the Taylor assumption and prescription of isothermal or adiabatic conditions are enforced here only for the purpose of calibrating material parameters in conjunction with a material point simulator (i.e., a finite element mesh consisting of a single element). In later parts of the present work, polycrystalline aggregates are modeled with numerous finite elements per crystal, inter- and intragranular interactions are taken into account, inertial forces participate, and heat conduction is permitted throughout the domain.

Fig. 2 shows isothermal stress–strain curves for uniaxial compression of 300 pure W grains of random initial lattice orientations. Notice that here we deform the crystal(s) in uniaxial compression in the 2-direction, i.e. $f_2^2 = 1 - \dot{\epsilon}t$, with $\dot{\epsilon}$ the prescribed nominal strain rate. The macroscopic logarithmic (true) strain is then defined by $\bar{\epsilon} \equiv -\ln(f_2^2)$, while $\bar{\sigma} \equiv V^{-1} \int \sigma^{22} dV$, with V the total reference configuration volume of the polycrystal, equally partitioned into 300 grains. Results correspond to the strain-hardening model outlined in Eqs. (25) and (26), with material parameters for single crystalline W shown in column 2 of Table 1. Values of $g_y^{(x)} = g_0^{(x)}|_{t=0}$, A , and B in Eq. (25) were chosen based upon the quasi-static data for polycrystalline W given by Dümmer et al. (1998), while a relatively large value of $q = 1.4$ was selected for use in Eq. (26) following the discussion on latent hardening in W single crystals by Horwath (1994). The strain rate and thermal sensitivity parameters, m and p respectively, were obtained from the crystal plasticity model for pure W of Lee et al. (1999). The mass density in the reference configuration is written as ρ_0 , and values of temperature-dependent material properties (e.g., elastic moduli) correspond to a reference temperature of 300 K. Strong strain rate sensitivity of the flow stress is evident in Fig. 2.

Fig. 3 shows isothermal shear stress–strain behavior of the pure matrix phase, calculated from the response of 300 randomly oriented grains. Shearing was conducted in the 1–2 plane, i.e., $f_2^1 = 1 + \dot{\gamma}t$. The macroscopic accumulated shear strain was then found simply as $\bar{\gamma} = \dot{\gamma}t$, while $\bar{\tau} \equiv V^{-1} \int \sigma^{12} dV$. Constants A and B in Eq. (25) and initial conditions $g_y^{(x)} = g_0^{(x)}|_{t=0}$ were chosen to fit the quasi-static ($\dot{\gamma} = 10^{-4}$) torsion data of Zhou (1993), and are shown in column 3 of Table 1, along with the other material parameters for the matrix phase. The strain rate sensitivity exponent was assumed to be the same as the pure W grains following the experimental data of Zhou (1993). We also selected $\dot{\gamma}_0$ to match the value for the pure W, and used Taylor's (1934) latent hardening assumption typical for FCC metals,

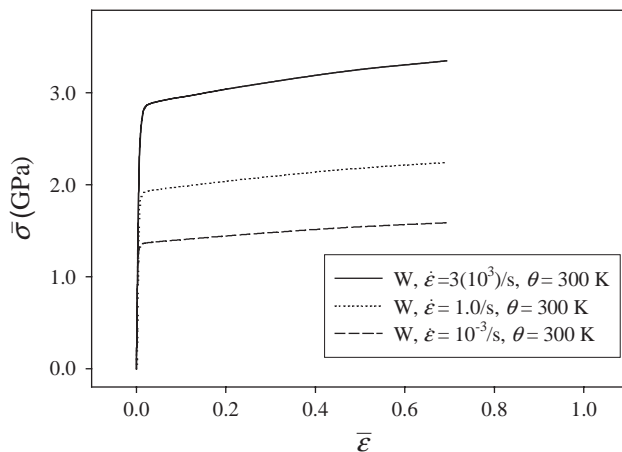


Fig. 2. Average axial stress vs. compressive true strain for W, isothermal conditions, 300 grains, Taylor model.

Table 1
Material parameters

Parameter	Value (W)	Value (Matrix)
λ	204 GPa	137 GPa
μ	161 GPa	99 GPa
ρ_0	19350 kg/m ³	9200 kg/m ³
\hat{c}	134 J/(kg K)	382 J/(kg K)
$\dot{\gamma}_0$	0.001	0.001
m	20	20
q	1.4	1.0
A	630 MPa	200 MPa
B	1.5	0.4
$g_y^{(z)}$	500 MPa	150 MPa
p	−1.5	−1.5
θ_0	300 K	300 K
α_T	$5.3(10)^{-6}/\text{K}$	$1.5(10)^{-5}/\text{K}$
k	160 W/(m K)	100 W/(m K)
$\hat{\alpha}$	0.38	0.73
b	0.318 nm	0.364 nm
κ	1000	100

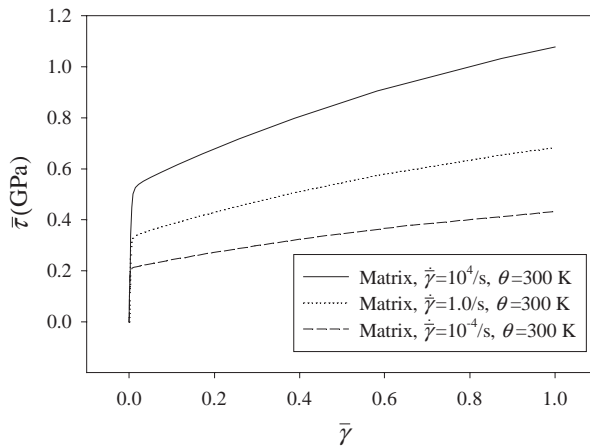


Fig. 3. Average shear stress vs. shear strain for matrix, isothermal conditions, 300 grains, Taylor model.

$q = 1.0$. Note also that the parameters $\hat{\alpha}$ and κ —associated herein with stored energy of cold working—need not be specified in order to conduct an isothermal stress–strain prediction.

For the purpose of conducting adiabatic analyses, additional calibrations were needed to determine values of $\hat{\alpha}$ and κ for each material, requiring particular assumptions on the nature of stored energy of cold work. Manipulating Eq. (23) and

then differentiating with respect to time give, respectively,

$$\dot{\xi} \equiv b\sqrt{\rho_T} = \frac{\tilde{\rho}\partial_{\xi}\psi}{\kappa\mu} = \frac{1}{\hat{\alpha}\mu n} \sum_{\alpha=1}^n (g_0^{(\alpha)} - g_y^{(\alpha)}), \quad \dot{\xi} = b \frac{\dot{\rho}_T}{2\sqrt{\rho_T}} = \frac{1}{\hat{\alpha}\mu n} \sum_{\alpha=1}^n \dot{g}_0^{(\alpha)}. \quad (34)$$

Additionally,

$$\tilde{\rho}\theta(\partial_{\theta\xi}\psi) = \theta\partial_{\theta}(\kappa\mu b\sqrt{\rho_T}) = \kappa\theta(\partial_{\theta}\mu)(b\sqrt{\rho_T}) = \frac{\kappa\theta(\partial_{\theta}\mu)}{\hat{\alpha}\mu n} \sum_{\alpha=1}^n (g_0^{(\alpha)} - g_y^{(\alpha)}). \quad (35)$$

Substituting Eqs. (34) and (35) into Eq. (29) then yields

$$\beta = 1 - \frac{\kappa(\mu + \theta(\partial_{\theta}\mu))}{(\hat{\alpha}\mu n)^2} \left[\sum_{\alpha=1}^n (g_0^{(\alpha)} - g_y^{(\alpha)}) \sum_{\alpha=1}^n \dot{g}_0^{(\alpha)} \right] \left[\sum_{\alpha=1}^n \tilde{\tau}^{(\alpha)} \dot{\gamma}^{(\alpha)} \right]^{-1}. \quad (36)$$

The dislocation density variable can be determined from Eq. (34) once $\hat{\alpha}$ is known, i.e.,

$$\rho_T = \left[\frac{1}{\hat{\alpha}\mu n b} \sum_{\alpha=1}^n (g_0^{(\alpha)} - g_y^{(\alpha)}) \right]^2. \quad (37)$$

Notice that Eq. (37) is a convenient relationship between the total dislocation density ρ_T and the hardness $g_0^{(\alpha)}$ averaged over all n potential slip systems at reference temperature θ_0 . The value of parameter $\hat{\alpha}$ can be selected based upon experimentally obtained measurements of the dislocation line density. Following such a procedure, we selected a value of $\hat{\alpha}$ by comparing simulated isothermal results for the dislocation density ρ_T in [1 0 0] and [1 1 2] W crystals with the experimental data of [Argon and Maloof \(1966\)](#) on single crystals deformed quasi-statically under uniaxial tension. We chose our value of $\hat{\alpha}$ for the matrix alloy by matching the dislocation evolution in randomly oriented 300 grain polycrystals of pure W and matrix materials. [Nix and Gao \(1998\)](#) used a value of $\hat{\alpha} = 0.5$ for copper and silver crystals, close to our values of 0.38 and 0.73 for W and matrix materials, respectively, as listed in [Table 1](#). It should be noted that since the experimental data we used to justify our choice of $\hat{\alpha}$ suffers from an acknowledged lack of precision ([Argon and Maloof, 1966](#)), our variable ρ_T should be viewed in the present study as a qualitative, yet physically-based, measure useful for comparing the relative degree of strain hardening accumulated in regions of W and matrix phases.

If data revealing evolution of β is available from physical experiments (cf. [Hodowany et al., 2000; Rosakis et al., 2000](#)), Eq. (36) can be inverted to deduce an appropriate value of the parameter κ . Vice-versa, if κ is known, then instantaneous values of β can be predicted via Eq. (36). It is apparent from (20) and (36) that $\beta \rightarrow 1$ as $\kappa \rightarrow 0$, meaning no energy of crystal defects is stored in the lattice when $\kappa = 0$. Caution must be used when selecting a value of κ such that $\beta \geq 0$ at all times (approximately, in an adiabatic analysis) in order to satisfy the reduced dissipation inequality (15). [Fig. 4](#) shows the average value $\bar{\beta} \equiv V^{-1} \int \beta dV$ for randomly oriented polycrystals of each phase deformed in uniaxial compression, assuming fixed values of κ for each analysis ([Table 1](#)) such that $0.8 \lesssim \bar{\beta} \leq 1.0$ throughout the

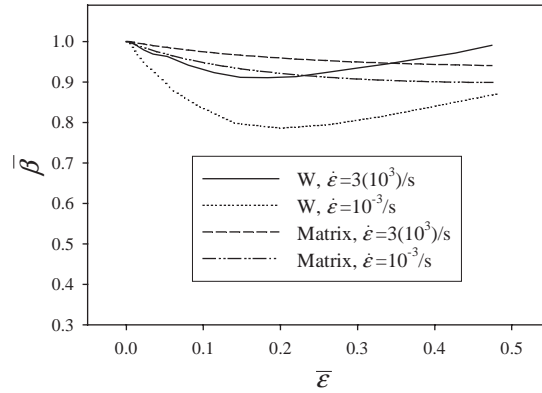


Fig. 4. Average cold work parameter, adiabatic compression, 300 grains, Taylor model.

deformation history. Subhash et al. (1994a) estimated from infrared temperature measurements that $\bar{\beta}$ approached unity in their high-rate compression tests on pure W polycrystals, while Zhou and co-workers (Zhou et al., 1994; Zhou, 1998a, b) used $\bar{\beta} = 0.9$ for matrix and pure W phases in dynamic finite element calculations. Notice that instantaneous values of $\bar{\beta}$ depend strongly upon the form of the rate equations for the slip resistances $g_0^{(x)}$, the latter which, upon consideration of Eq. (34), can also be viewed as evolution equations for the defect density. For the pure W phase, we notice that $\bar{\beta}$ decreases with strain to a minimum value around $\bar{\epsilon} = 0.2$, then increases due to the relatively large rate of dynamic recovery dictated by the choice of $B = 1.5$ in Eq. (25). In contrast, for the more steadily hardening matrix phase ($B = 0.4$), $\bar{\beta}$ decreases continuously with increasing strain. Please notice that we include the slow-rate adiabatic data in Fig. 4 for illustrative purposes, in order to make our presentation complete, since conventionally (nearly) adiabatic conditions are achieved only at relatively high rates of loading.

Figs. 5 and 6 depict the stress–strain behavior and temperature histories of both materials under adiabatic test conditions, where we have used an initial temperature of 300 K. The volume-averaged temperature is written as $\bar{\theta}$. For the matrix phase, upon using the data of Zhou (1993) to estimate an average thermal softening rate $\partial_{\bar{\theta}} \bar{\tau}$, we selected the same values for thermal softening parameters p and θ_0 (Table 1) as used for the W phase.

Significant heating and thermal softening is apparent in the W material, especially at the higher strain rate ($\dot{\epsilon} = 3000/s$) where the plastic dissipation is relatively large. Again, curves for slow-rate adiabatic tests are included for illustrative purposes, with thermal softening evident in the W grains even at an applied strain rate of $\dot{\epsilon} = 10^{-3}/s$. Comparing Figs. 3 and 5, the relatively strong rate of strain hardening due to dislocation accumulation in the matrix phase is counteracted by thermal softening under adiabatic conditions. Notice that, for a given strain rate, the temperature rise in the W grains tends to exceed that in the matrix, in part because of the much larger specific heat parameter (\hat{c}) of the latter. The melting temperature of

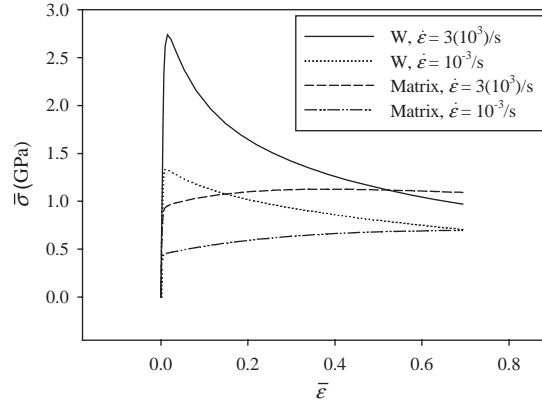


Fig. 5. Average axial stress vs. compressive true strain, adiabatic compression, 300 grains, Taylor model.

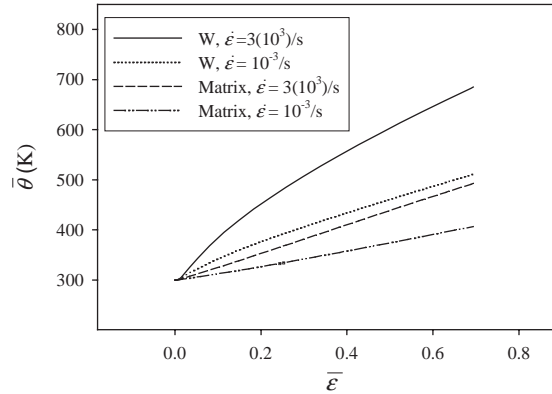


Fig. 6. Average temperature vs. compressive true strain, adiabatic conditions, 300 grains, Taylor model.

pure W is 3410 K (Boyer and Gall, 1985) while that of the matrix is approximately 1750 K (Zhou and Clifton, 1997). Neither material attained its melting point in our simulations.

3. Fracture modeling

As discussed by Weerasooriya (2003), failure of WHA specimens subjected to high rates of macroscopic tensile deformation often initiates via local fracture at W–W (i.e., grain–grain) interfaces, and less often at interfaces between W grains and the matrix phase. The former interfaces are thought to be weaker than the latter, based upon visual examination of recovered specimens which demonstrate that fracture surfaces are prone to initiate at W–W boundaries and then either propagate along

W-matrix interfaces, or less often, along cleavage planes within grains of either phase (Zamora et al., 1992; Weerasooriya et al., 1994; O'Donnell and Woodward, 2000; Woodward and O'Donnell, 2000; Weerasooriya, 2003).

Consistent with these experimental observations, in our simulations cracks are generated at interfaces between grains of the same or different phases: W–W grain boundaries and W-matrix boundaries. Intragranular cracking and fracture at matrix–matrix grain boundaries are not captured, as these failure modes were observed less frequently in the aforementioned high-rate experiments (Weerasooriya et al., 1994; Weerasooriya, 2003) and in the room temperature, quasi-static experiments of Woodward and O'Donnell (2000). The dynamic finite element approach is employed, with new fracture surfaces generated at interfaces between continuum elements when the traction acting upon the potential initiation site exceeds the intrinsic failure strength of the interface (a material parameter). Hence, fracture at interfaces initiates when one of the following local stress-based criteria is attained:

$$\hat{s} = \hat{s}_0, \quad \hat{\tau} = \hat{\tau}_0, \quad (38)$$

where \hat{s} and $\hat{\tau}$ are the resolved normal traction and shear traction on the interfacial surface, measured per unit reference configuration area, and \hat{s}_0 and $\hat{\tau}_0$ are material parameters specifying the normal and tangential (i.e., mode I and mode II) fracture strengths of the interface. In the finite element implementation, duplicate nodes are generated along all potential fracture surfaces during the meshing stage. Initially coincident nodes are then constrained to share the same velocity and temperature histories until either of conditions (38) is reached.

After initiation of fracture, the constitutive response of the degraded material (i.e., within the cohesive zones) at the interfaces is dictated by the following set of coupled irreversible traction-displacement relationships (see e.g. Camacho and Ortiz, 1996):

$$\begin{aligned} \hat{s} &= \hat{s}_0 \left(1 - \frac{\delta_n}{\delta_c} \right) \quad (\text{loading}), \\ \hat{s} &= \hat{s}_0 \left(1 - \frac{\delta_{n1}}{\delta_c} \right) \frac{\delta_n}{\delta_{n1}} \quad (\text{unloading}), \end{aligned} \quad (39)$$

$$\begin{aligned} \hat{\tau} &= \hat{\tau}_0 \left(1 - \frac{|\delta_t|}{\delta_c} \right) \left(1 - \frac{\langle \delta_n \rangle}{\delta_c} \right) \text{sgn}(\delta_t) \quad (\text{loading}), \\ \hat{\tau} &= \hat{\tau}_0 \left(1 - \frac{|\delta_{t1}|}{\delta_c} \right) \left(1 - \frac{\langle \delta_n \rangle}{\delta_c} \right) \frac{\delta_t}{|\delta_{t1}|} \quad (\text{unloading}), \end{aligned} \quad (40)$$

where δ_n and δ_t are the normal and tangential crack opening displacements, δ_{n1} and δ_{t1} are the maximal values of δ_n and δ_t achieved during prior loading, and δ_c is a material parameter describing the separation distance at which the cohesive interface no longer supports traction (i.e., critical opening displacement for total failure). The Macaulay bracket is written $\langle x \rangle$, satisfying $\langle x \rangle = x \forall x \geq 0$ and $\langle x \rangle = 0 \forall x < 0$. As shown in Fig. 7(a) for pure tension and Fig. 7(b) for pure shear, unloading (reloading) occurs linearly to (from) the origin in traction-displacement space. Also

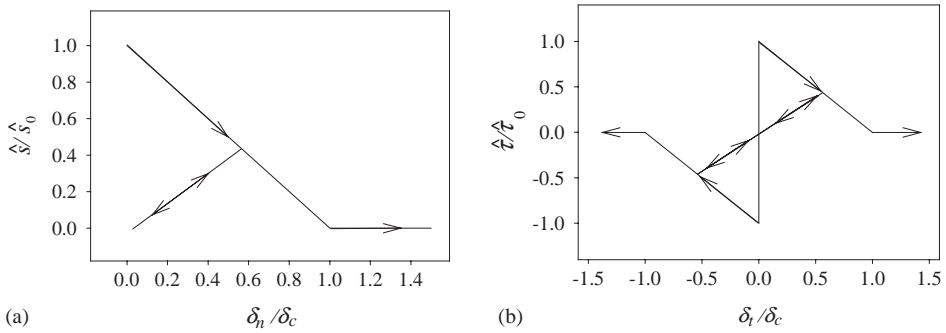


Fig. 7. Cohesive traction-displacement behavior for pure tension (a) and pure shear (b).

prior to attainment of fracture criteria (38), heat conduction across interfaces is permitted. Upon initiation and subsequent normal separation beyond δ_c , however, we enforce the null heat flux conditions $\nabla_x \theta \cdot \mathbf{n} = 0$, where \mathbf{n} is the outward normal vector to the newly-created fracture surface.

It should be noted that the rate- and temperature-independent traction-separation laws described in relations (38)–(40) were chosen because of their wide acceptance in the literature and their relative simplicity, requiring few material-dependent fracture properties. Particular choices of values of these properties are discussed in the next Section. More elaborate, and potentially more physically realistic, cohesive constitutive models have been advanced in the recent literature for a variety of material systems, and dynamic fracture predictions are known to exhibit sensitivity to the particular choice of cohesive law (Falk et al., 2001). However, as will be discussed more in the next Section, the fracture properties of the local interfaces in the WHA material system are difficult to characterize experimentally (Woodward and O'Donnell, 2000), and even the macroscopic fracture toughness of the alloy is not known with great precision, as is evident by the broad range of values reported in the literature (Zamora et al., 1992). Regarding relations (38), ratios of $\hat{\tau}_0/\hat{\sigma}_0$ deviating from unity were not explored in the present study, nor were mixed-mode initiation criteria. Such limiting assumptions were deemed acceptable for the present set of uniaxial tensile simulations, in which mode I fractures dominated, though we anticipate extending our framework in the future to explore the influence of mixed-mode activation criteria on predicted fracture patterns. Exploration of temperature- and strain-rate-dependence of the cohesive laws (cf. Costanzo and Walton, 2002), and statistical variations in cohesive strengths among interfaces (Espinosa and Zavattieri, 2003a, b; Zhou and Molinari, 2004) is beyond the scope of the present effort, and beyond the support of the limited available experimental data of the WHA material system under consideration. Parametric investigations probing these phenomena, as well as effects of choice of various traction-separation curve shapes (cf. Bjerke and Lambros, 2003) and coupling schemes between normal and tangential traction-separation relations (Ortiz and Pandolfi, 1999; Espinosa and Zavattieri, 2003b) are reserved for future work.

4. Finite element simulations: two-phase microstructure

4.1. Numerical procedures

The constitutive models presented in Sections 2 and 3 for thermo-elastoplasticity of each of the WHA phases and interfacial fracture were implemented within the EPIC dynamic wave propagation finite element solver (Johnson et al., 1997, 2001). In this approach, the equations of motion, i.e. the second of Eqs. (6), are integrated directly and explicitly using the algorithm of Belytschko et al. (1976). The deformation gradient is then updated within each element as

$$\mathbf{f}_{t+\Delta t} = \exp(\mathbf{I}\Delta t)\mathbf{f}_t, \quad (41)$$

where $\mathbf{I} = \dot{\mathbf{f}}\mathbf{f}^{-1}$ is the velocity gradient that is assumed constant over the time interval $(t, t + \Delta t)$. The constitutive update proceeds within each element via the methodology discussed in Section 2.5. Contributions to the energy balance (19) from plastic dissipation, lattice defects, and thermoelastic coupling are calculated, and then the temperature field is updated following the explicit integration procedure of Johnson (1981). Possible contributions from cohesive elements to global mechanical and thermal force vectors are accounted for just prior to the enforcement of boundary conditions and initiation of the integration step for the deformation field of the next cycle. The stable time increment for each cycle is chosen as a small fraction of the time required for a longitudinal elastic stress wave to traverse the smallest element in the grid.

Results from two different 2D meshes, shown in Figs. 8(b) and 8(c), reconstructed from an optical micrograph of a sectioned microstructure obtained from an undeformed WHA sample (Fig. 8(a)), will be discussed in the present work. The meshes consist of constant strain triangular elements, generated with the PPM2OOF software package (Langer et al., 2003), readily enabling refinement along material interfaces (i.e., mesh refinement along potential cohesive fracture surfaces). The grid in Fig. 8(c) was generated by rotating that in Fig. 8(b) by 90° , with the latter a direct reproduction of the image shown in Fig. 8(a). The square domain is of size $L = 150 \mu\text{m}$, and the area fraction of W–Ni–Fe matrix phase in each mesh is 12.6%.

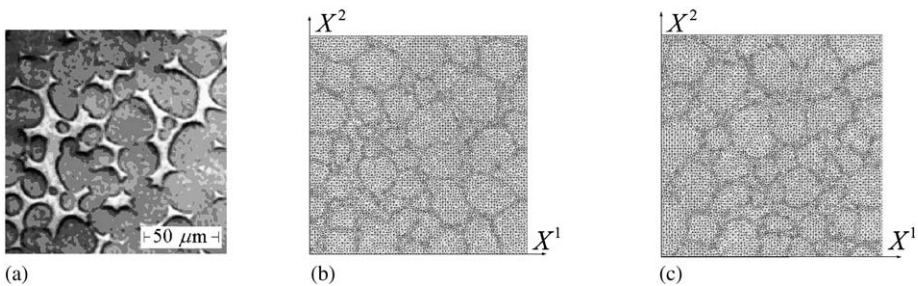


Fig. 8. Optical micrograph and finite element meshes of two-phase microstructure: (a) image, (b) mesh 1, (c) mesh 2.

Fifty distinct W grains are resolved, with grids consisting of a total of 16664 standard 3-node triangular elements and up to 1656 4-node cohesive finite elements inserted at potential fracture initiation sites along material interfaces.

We enforced the following boundary and initial conditions. Analyses were plane strain tension in the $x^1 - x^2$ plane, meaning that our simulations can be thought to represent columnar polycrystals extended infinitely in the out-of-plane direction. Please note that out-of-plane elastic and plastic deformations were permitted (i.e., the 3D material models discussed in Section 2 were employed, with the full number of slip systems enabling out-of-plane lattice rotations), so long as the total deformation field remained planar. Let the lower and upper edges of the domain be denoted by $X^2 = 0$ and $X^2 = L$, respectively. And let the left and right edges be denoted by $X^1 = 0$ and $X^1 = L$, respectively. The velocity boundary conditions are summarized as

$$\begin{aligned}\dot{x}^2 &= 0 \text{ along } X^2 = 0, \\ \dot{x}^2 &= 1.5 \text{ m/s along } X^2 = L, \\ \dot{x}^1 &= 0 \text{ at } (X^1 = L/2, X^2 = 0).\end{aligned}\tag{42}$$

Additionally, force boundary conditions were applied along the lateral edges $X^1 = 0$ and $X^1 = L$ such that these edges were constrained to remain straight and parallel, yet free to contract upon extension of the mesh in the x^2 -direction. These lateral edges were free of shear traction; i.e., $\sigma^{12} = 0$ along $X^1 = 0$ and $X^1 = L$. The sides were forced to remain straight in order to prevent necking or relative shearing of large sections of the mesh due to potentially highly localized deformation. Each lateral edge was constrained in practice by assigning a uniform acceleration \ddot{x}^1 to all nodes comprising the edge, with this value of \ddot{x}^1 calculated by dividing the total reaction force along the edge by the total mass of the nodes comprising the edge, a methodology similar to that employed by Zhou et al. (1994) for imposing periodic shear deformations. Such periodicity was also intended to instill the mesh with a global deformation mode representative of an actual element of material within a deforming test sample, i.e., a representative volume element (RVE). However, it is noted that we do not presume a priori that our volume of two-phase material contains a sufficient number of grains to satisfy the definition of an RVE in a strict sense (Hill, 1963). In order to minimize effects of tensile shock waves that would arise under impulsive loading, the following initial conditions were applied throughout the domain:

$$\dot{x}^2 = (1.5X^2/L) \text{ m/s at } t = 0.\tag{43}$$

Null heat flux boundary conditions were enforced as

$$\nabla_x \theta \cdot \mathbf{n} = 0 \text{ along } \begin{cases} X^1 = 0 \\ X^1 = L \\ X^2 = 0 \\ X^2 = L, \end{cases}\tag{44}$$

with \mathbf{n} the outward normal vector in the spatial frame, and an initial temperature $\theta_0 = 300$ K was prescribed uniformly throughout the problem domain. Conditions (42) result in an applied stretch rate of $\dot{\bar{\epsilon}} = 10^4/\text{s}$. Simulations were generally conducted for a total duration of $20\mu\text{s}$, producing a nominal stretch of $\bar{\epsilon} = 0.20$ at their conclusion. Total execution times averaged 960 CPU-hours divided among 10 parallel processors on a Silicon Graphics 3900 supercomputer. Please notice that tension simulations were of interest for the study of (predominantly) mode I fracture in the WHA material system, as this phenomena has not been probed numerically in previous computational investigations of this material's behavior (cf. Zhou et al., 1994; Zhou, 1998a, b). Note also that even though tension tests are simulated here, the constitutive models for plasticity in each phase of the material were calibrated primarily using experimental compression and torsion data, as data for tension is not readily available at higher strains and strain rates due to the relatively brittle nature of the material under such loading conditions.

Results from seven distinct simulations are discussed in the present work, listed as case numbers 1, 2, ... 7 in Table 2. For case 1, fractures were prohibited. Random initial lattice orientations for the W grains and matrix phase were assigned. Each pure W grain was assigned a different initial lattice orientation (i.e., set of Euler angles), while the entire matrix phase was assigned the same initial orientation, such that all 50 pure W grains were effectively embedded within a single "grain" of the matrix phase. In column 6 of Table 2, "1" refers to mesh 1 of Fig. 8(b). For case 2, all parameters were identical to those of case 1, except that fracture was permitted along W-matrix interfaces only, with a prescribed strength for opening of cohesive surfaces at such interfaces of $\hat{s}_0 = \hat{\tau}_0 = 2.0$ GPa. For case 3, all parameters were identical to those of case 1, except that fracture was permitted along W–W boundaries only, with a prescribed strength for opening of these cohesive surfaces of $\hat{s}_0 = \hat{\tau}_0 = 2.0$ GPa. For case 4, all parameters were identical to those of case 1, except that fracture was permitted along W–W boundaries and W-matrix interfaces, with a uniform initiation strength for opening of potential cohesive surfaces at all interfaces prescribed by $\hat{s}_0 = \hat{\tau}_0 = 2.0$ GPa. For case 5, all parameters were identical for those of case 4, except that the initial orientation of the lattice of the matrix phase was varied, as indicated by the value "2" in column 4 of Table 2 (an orientation with a

Table 2
Numerical simulations

Case	\hat{s}_0 , W–W (GPa)	\hat{s}_0 , W-matrix (GPa)	Matrix orientation	W orientations	Mesh (morphology)
1	∞	∞	1	1	1
2	∞	2.0	1	1	1
3	2.0	∞	1	1	1
4	2.0	2.0	1	1	1
5	2.0	2.0	2	1	1
6	2.0	2.0	1	2	1
7	2.0	2.0	1	1	2

significantly different Schmid factor relative to the other cases was used). For case 6, all parameters were identical to those of case 4, except that an alternate set of random initial lattice orientations was assigned to the 50 W grains, as indicated by the “2” in column 5 of Table 2. For case 7, all parameters were identical to those of case 4, except that mesh 2 of Fig. 8(c) was used. The same initial lattice orientations relative to the global specimen axes were used in cases 4 and 7.

We now discuss our choices of material parameters entering the cohesive relations (38)–(40). For simulations in which fractures were permitted, nominal values of $\hat{\sigma}_0 = \hat{\tau}_0 = 2.0$ GPa were assigned, in order to roughly match peak stress levels reported in experimental high-rate macroscopic data of Weerasooriya (2003), as will be discussed more later. Dandekar and Weisgerber (1999) estimated from plate impact experiments the spall threshold stress of WHA to lie between 1.7 and 2.0 GPa. In the actual material, stochastic variations in strength and toughness among interfaces are of course expected (Woodward and O'Donnell, 2000). Such variations are not addressed in the present work, but could be readily implemented within a cohesive finite element framework (Zhou and Molinari, 2004). A uniform value of $\delta_c = 1.0$ μm was chosen for the critical separation distance in the cohesive laws of Eqs. (39) and (40), a value thought to best represent the effective fracture properties of the WHA material system at the length scale resolved by the numerical discretization (i.e., at the scale of individual grains and their interfaces). Because the WHA alloys are highly heterogeneous, with fracture behavior dictated by microstructural features such as interfacial strengths and grain contiguity and influenced by large-scale yielding (i.e., finite plastic zones), difficulties arise in obtaining consistent measurements of the macroscopic fracture toughness, with values of $25 \leq K_{Ic} \leq 234$ $\text{MPa}\sqrt{\text{m}}$ reported by Zamora et al. (1992) and references therein. Furthermore, the microscopic fracture toughness of local interfaces is expected to be lower than that of the homogenized material, as recovered uniaxial test specimens reveal numerous microcracks that do not propagate to cause macroscopic rupture (Woodward and O'Donnell, 2000). Assuming that the material behaves linear-elastically and neglecting plastic dissipation which can dominate energy release in the cohesive zone (Rice and Wang, 1989), Woodward and O'Donnell (2000) estimated a static fracture toughness of $3.4 \leq K_{Ic} \leq 7.6$ $\text{MPa}\sqrt{\text{m}}$ for microcracking along interfaces within a WHA, while Dümmer et al. (1998) calculated values of $0.66 \leq K_{Ic} \leq 1.5$ $\text{MPa}\sqrt{\text{m}}$ for intergranular decohesion in pure polycrystalline W. The mode I fracture energy corresponding to our choices $\delta_c = 1.0$ μm and $\hat{\sigma}_0 = 2.0$ GPa is $G_c \equiv (1/2)\hat{\sigma}_0\delta_c = 1.0$ kJ, which, upon assuming for illustrative purposes only, an isotropic linear-elastic stress–strain response for the composite with an effective elastic modulus of $E = 3.66(10)^5$ MPa and a Poisson's ratio of $\nu = 0.29$ (Dandekar and Weisgerber, 1999), results in a plane strain fracture toughness of $K_{Ic} = \sqrt{G_c E / (1 - \nu^2)} = 20$ $\text{MPa}\sqrt{\text{m}}$, which we feel is an acceptable compromise among the aforementioned ranges of values reported in the literature. Note also that our value of δ_c is slightly larger than but of the same order of magnitude of the characteristic length of a typical bulk finite element within the mesh, which we found of adequate resolution to facilitate stable, converged solutions. Cohesive elements were deemed of sufficiently small size to resolve the

process zone, the length of which may be liberally estimated again assuming a linear elastic bulk response (cf. Rice, 1968; Espinosa and Zavattieri, 2003b).

4.2. Numerical results

Contour plots of solution field variables corresponding to cases 1–7 are given in Figs. 9–15, respectively, all corresponding to $t = 10 \mu\text{s}$, or an applied tensile strain of $\bar{\varepsilon} = 0.10$. In part (a) of each figure, the effective deviatoric stress σ_e referred to the spatial frame is defined by

$$\sigma_e \equiv \sqrt{3/2(\boldsymbol{\sigma} - 1/3\text{tr}(\boldsymbol{\sigma})\mathbf{1}) : (\boldsymbol{\sigma} - 1/3\text{tr}(\boldsymbol{\sigma})\mathbf{1})}, \quad (45)$$

while the scalar effective plastic strain ε_p of part (b) of each figure is found by

$$\varepsilon_p \equiv \int \sqrt{(2/3)\mathbf{d}^p : \mathbf{d}^p} dt, \quad (46)$$

where $2\mathbf{d}^p \equiv \dot{\mathbf{p}} + \dot{\mathbf{p}}^T$ is the rate of plastic stretching referred to the spatial configuration. Part (c) of each figure shows the absolute temperature θ , part (d) gives the dislocation density ρ_T introduced in Eq. (23), and part (e) illustrates instantaneous values of the plastic work-to-heat conversion parameter β of Eqs. (29) and (36).

Consider first the damage-free case 1, with contours given in Fig. 9. From Fig. 9(a), we notice that the W grains generally support higher effective stress than the W–Ni–Fe matrix phase. From Fig. 9(b), the opposite is true regarding effective plastic strain, with the matrix phase accommodating more of the total applied stretch. Also, as seen in Fig. 9(c), the temperature rise is greatest in regions of the matrix phase relative to that in the W grains, as a result of relatively greater plastic deformation and subsequent conversion to heat energy in the former. Clearly, over the short duration of the simulation ($t = 10 \mu\text{s}$ in Fig. 10), heat energy does not have time to diffuse uniformly throughout the material via conduction. As seen in Fig. 9(d), dislocation activity is also concentrated in matrix regions, as the ductile phase undergoes more straining, more strain hardening, and more dislocation accumulation than the W phase. Fig. 9(e) shows β , which can be thought of as a snapshot of dislocation accumulation rates at the selected time of $t = 10 \mu\text{s}$. The greater the value of β at a particular time instant, the lesser the rate of local strain hardening and associated dislocation accumulation, and the greater the fraction of plastic dissipation converted into a temperature rise. Regions of relatively high and low values of β are not restricted to one particular phase in the material, indicating that plastic straining and dislocation accumulation are occurring non-uniformly throughout the sample at $t = 10 \mu\text{s}$.

We now discuss the results for the elastic–plastic–fracture simulations shown in Figs. 10–15 collectively and relative to those of Fig. 9. Considering the stress contours (part (a) of each figure), it is clear that stresses are reduced on average as a result of microcracking, though local stress concentrations in excess of $\sigma_e = 3.0 \text{ GPa}$ are present in all cases. The net stress reduction is greatest in cases 4–7, which permit fracture at all interfaces, as opposed to cases 2 and 3, in which fracture is only

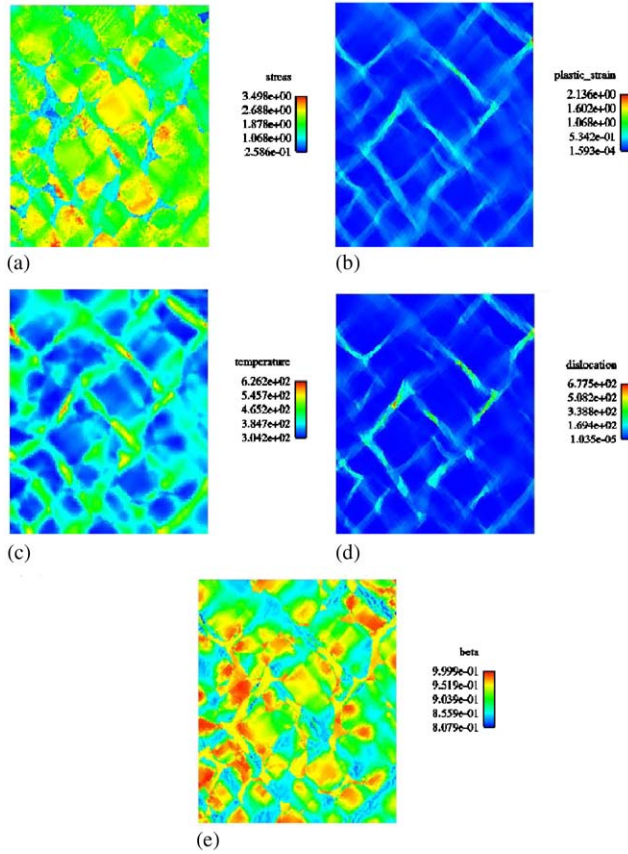


Fig. 9. Contours of results at applied stretch of $\bar{\epsilon} = 0.10$ for case 1: (a) effective stress σ_e (GPa), (b) effective plastic strain ε_p , (c) temperature θ (K), (d) dislocation density ρ_T ($\times 10^{-7}/\text{cm}^2$), (e) heat dissipation parameter β .

permitted at W-matrix or W–W interfaces, respectively. Homogenized stress–strain curves for the material samples will be discussed more later. Comparing Fig. 9(b) with Figs. 10(b)–15(b), damage in the form of microcracking accommodates much of the inelastic deformation that would otherwise be accommodated by plastic straining in the matrix phase. Contours of effective plastic strain in Figs. 10(b)–15(b) are calibrated to show a maximum value of $\varepsilon_p = 2.0$, with all regions exhibiting strains greater than this value red in color. In the calculations for cases 2–7, we imposed an element-based failure criterion in addition to the cohesive fracture model, removing severely distorted elements from the global mechanical and thermal force balances and the stable time step estimation calculation upon attainment of very large local strains, specifically when $\varepsilon_p > 10.0$. This criterion permitted us to continue the simulations to large applied strain levels and also allowed some cracks to propagate through regions of bulk material. This element failure criterion is justified by the fact that the most severely distorted elements tend to have undergone significant thermal

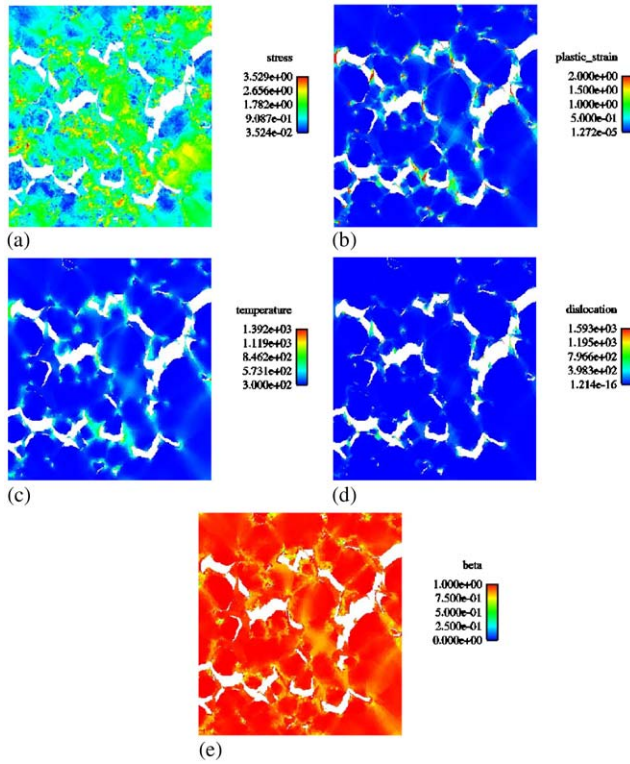


Fig. 10. Contours of results at applied stretch of $\bar{\epsilon} = 0.10$ for case 2: (a) effective stress σ_e (GPa), (b) effective plastic strain ϵ_p , (c) temperature θ (K), (d) dislocation density ρ_T ($\times 10^{-7}/\text{cm}^2$), (e) heat dissipation parameter β .

softening as a result of intense plastic deformation, and hence carry relatively little stress prior to their removal. This element failure criterion was not used for case 1. As is clear from parts (b), (c), and (d) of Figs. 10–15, intense plastic strain, temperature rise, and dislocation accumulation are concentrated in the matrix phase and within relatively distorted regions of the W grains in the vicinity of failed interfaces. From part (e) of Figs. 10–15, β approaches unity throughout most of the domain in each case, although scattered regions with relatively low values of β , indicating instantaneous strain hardening activity, are evident in each figure.

Different microcrack patterns and fracture paths are evident for each of cases 2–7, as is clear from Figs. 10–15. The most notable differences arise in cases 2 and 3 (Figs. 10 and 11, respectively) relative to cases 4–7, Figs. 12–15. Potential fracture paths are impeded in cases 2 and 3 relative to cases 4–7, because of the limitation in the former of crack propagation to either W-matrix or W–W boundaries exclusively. In cases 4–7, propagation of damage is less inhibited and mode I crack(s) are able to propagate more readily across the entire domain. Thus our simulated cases 4–7 most closely replicate the hypotheses of Woodward and O'Donnell (2000) and

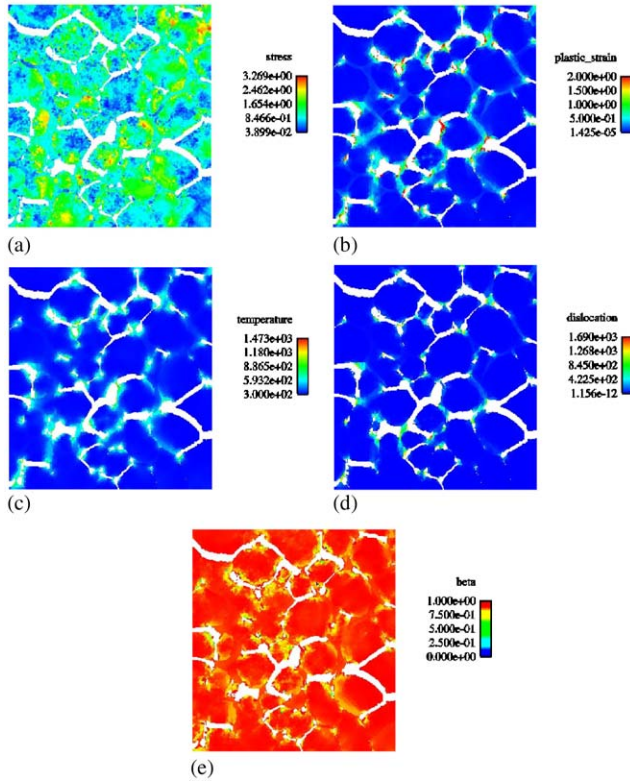


Fig. 11. Contours of results at applied stretch of $\bar{\epsilon} = 0.10$ for case 3: (a) effective stress σ_e (GPa), (b) effective plastic strain ε_p , (c) temperature θ (K), (d) dislocation density ρ_T ($\times 10^{-7}/\text{cm}^2$), (e) heat dissipation parameter β .

Weerasooriya (2003), who suggested that cracks initiate primarily at the weakest W–W grain boundaries and grow subsequently by following trajectories of minimum resistance, in our simulations along interconnected W–W and W-matrix interfaces. Comparing Fig. 11 with Fig. 12, it is clear that limiting crack growth to W–W interfaces alone severely restricts macro-crack propagation relative to the case when both W–W and W-matrix fractures are permitted simultaneously. If we view our aggregate of material as statistically representative, this result suggests that W-matrix interface failures (or intragranular failures) must take place for macro-crack propagation in the actual material, as the W–W boundaries alone cannot account for propagation across more than a few dozen micrometers, as limited by the occurrence of continuously linked W–W grain boundaries. Also from Figs. 12–14, we notice that random changes in lattice orientation of W grains or the matrix phase do affect the distribution of damage, stress, and deformation within each sample, though dominant cracks with similar paths traverse the upper and lower thirds of each mesh in all of these cases.

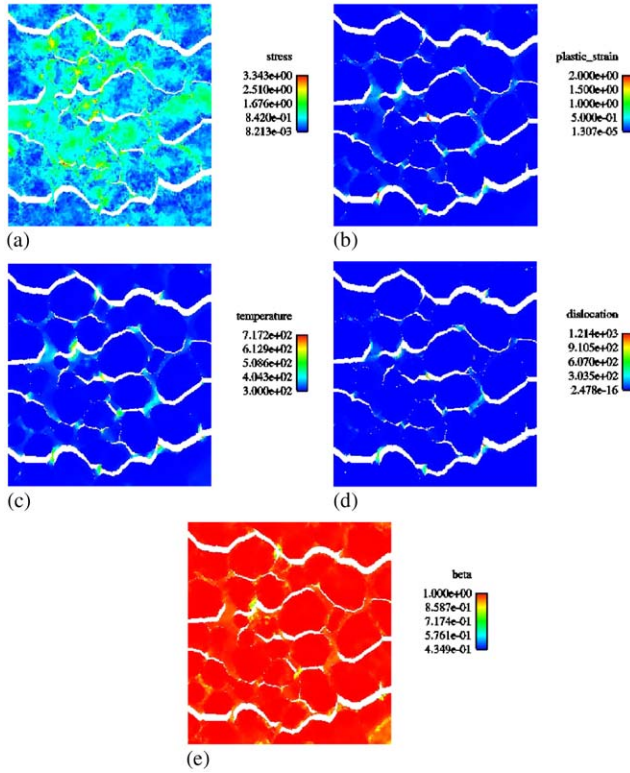


Fig. 12. Contours of results at applied stretch of $\bar{\epsilon} = 0.10$ for case 4: (a) effective stress σ_e (GPa), (b) effective plastic strain ε_p , (c) temperature θ (K), (d) dislocation density ρ_T ($\times 10^{-7}/\text{cm}^2$), (e) heat dissipation parameter β .

Table 3 provides the time instant, cohesive element number, and interface type corresponding to the initiation of damage in each simulation. Data in Table 3 correspond to satisfaction of initiation conditions (38) and not total stress relief in the cohesive zones. We see that damage initiation occurs very early in each case ($t \approx 0.3 \mu\text{s}$, at an applied stretch of $\bar{\epsilon} \approx 0.3\%$), and always at a W–W interface when possible (recall that W–W interface fractures were prohibited for case 2). Significantly, first fracture initiated at W–W interfaces even when all interfaces were given the same strength of 2.0 GPa, as in cases 4–7. This is expected considering our prior observation that the W grains tend to carry higher stresses than the matrix material, meaning that stresses should be relaxed at typical W–matrix interfaces relative to W–W interfaces. Since fracture occurred at the same location and virtually the same time instant for each of cases 3–6, we deduce that the deformation at this point throughout the mesh was nearly (thermo)elastic, since elastic isotropy was enforced for each phase. However, since the first fracture in case 5 took place slightly later than that of cases 3, 4, and 6, some minor plastic deformation probably occurred in the matrix material preceding the first fracture. Recall that case 7 is a

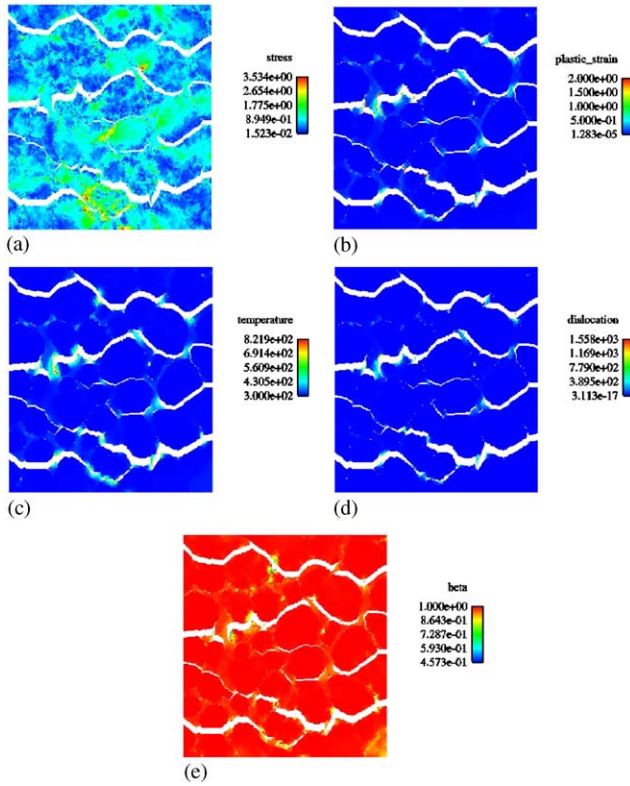


Fig. 13. Contours of results at applied stretch of $\bar{\epsilon} = 0.10$ for case 5: (a) effective stress σ_e (GPa), (b) effective plastic strain ϵ_p , (c) temperature θ (K), (d) dislocation density ρ_T ($\times 10^{-7}/\text{cm}^2$), (e) heat dissipation parameter β .

different mesh than cases 2–6, hence a different cohesive element failed first in the former simulation, as would be expected.

Table 1 and Figs. 10–15 point to design protocols for W alloys that could result in improved resistance to failure. It is suggested that by improving the fracture strengths of the W–W interfaces, or by reducing their relative frequency, fracture may be delayed. Such a conjecture agrees with the experiments of Weerasooriya et al. (1994), who were able to achieve increases in strain-to-failure by reducing the contiguity of W grains (and thereby the frequency of W–W boundaries) in WHAs deformed in high rate torsion tests in a Kolsky bar apparatus. Furthermore, our results suggest that by increasing the strength of one type of interface relative to the other, and thereby limiting fracture to just a single mechanism (i.e., only one type of interface, and no intragranular failure), macro-crack propagation may be severely impeded.

Fig. 16 presents average effective stress–strain data for each of the simulations, $\bar{\sigma}_e \equiv V^{-1} \int \sigma_e dV$, with V the total volume of the problem domain in the reference

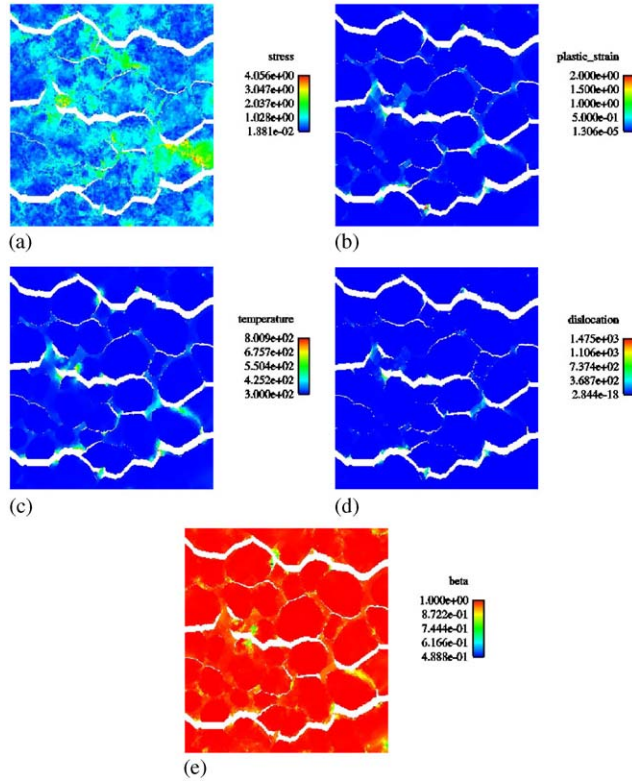


Fig. 14. Contours of results at applied stretch of $\bar{\epsilon} = 0.10$ for case 6: (a) effective stress σ_e (GPa), (b) effective plastic strain ϵ_p , (c) temperature θ (K), (d) dislocation density ρ_T ($\times 10^{-7}/\text{cm}^2$), (e) heat dissipation parameter β .

configuration. In the legend of Fig. 16, case labels of each simulation consistent with the identifiers listed in Table 2 are indicated in parentheses. Data for the damage-free case 1 is given only over the range $0.0 \leq \bar{\epsilon} \leq 0.10$, since an element failure criterion was not used in that particular simulation. The simulation was halted at this strain level due to highly distorted elements in the vicinity of a localized deformation zone sustaining significant heating. For the remaining cases 2–7, data is shown over the applied strain range $0.0 \leq \bar{\epsilon} \leq 0.20$. For case 1, a peak stress of $\bar{\sigma}_e = 2.55$ GPa occurs at an applied stretch of $\bar{\epsilon} = 0.024$, beyond which the average stress decreases as a result of temperature rise and commensurate thermal softening. Average stress values are significantly reduced in cases 2–7 relative to case 1 as a result of damage (i.e., material separation at cohesive interfaces). For case 2, in which fracture is restricted to W-matrix interfaces, a peak average stress of $\bar{\sigma}_e = 1.98$ GPa is attained at an applied stretch of $\bar{\epsilon} = 0.012$. For case 3, with fracture allowed at W–W interfaces only, a peak stress of $\bar{\sigma}_e = 1.93$ GPa is reached at $\bar{\epsilon} = 0.010$. Cases 4–7, in which all interfaces support potential fracture, exhibit very similar average stress–strain behavior, with maximum stresses of $\bar{\sigma}_e \approx 1.52$ GPa attained at a stretch

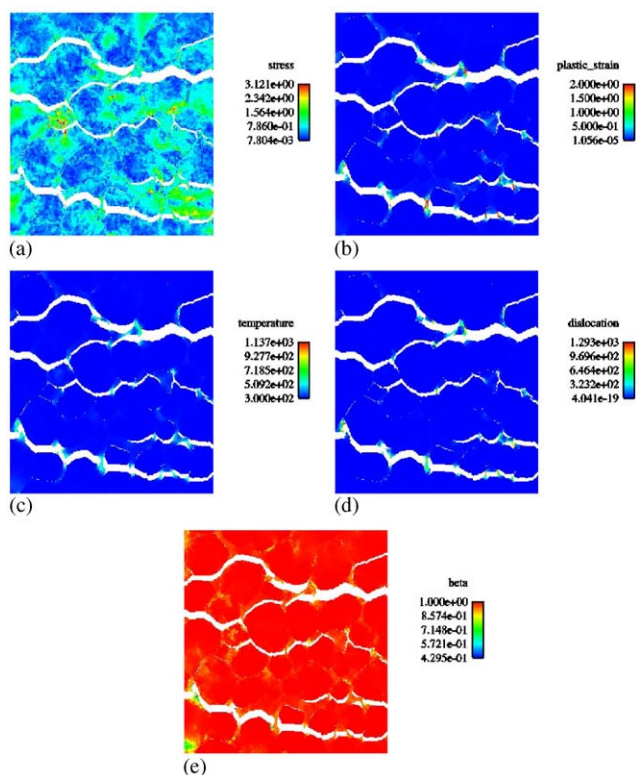


Fig. 15. Contours of results at applied stretch of $\bar{\epsilon} = 0.10$ for case 7: (a) effective stress σ_e (GPa), (b) effective plastic strain ϵ_p , (c) temperature θ (K), (d) dislocation density ρ_T ($\times 10^{-7}/\text{cm}^2$), (e) heat dissipation parameter β .

Table 3
Times and locations of initial fractures

Case	Time (μs)	Element #	Interface type
2	0.3375	146	W-matrix
3	0.3122	1309	W-W
4	0.3122	1309	W-W
5	0.3132	1309	W-W
6	0.3122	1309	W-W
7	0.3039	1227	W-W

of $\bar{\epsilon} \approx 0.008$ in each simulation. From these results we arrive at the rather obvious conclusion that increasing the available fracture sites in the sample results in a greater reduction in effective stiffness and the attainment of a peak average stress at a lower value of applied strain. Also notice from the similarity of curves for cases 4–7

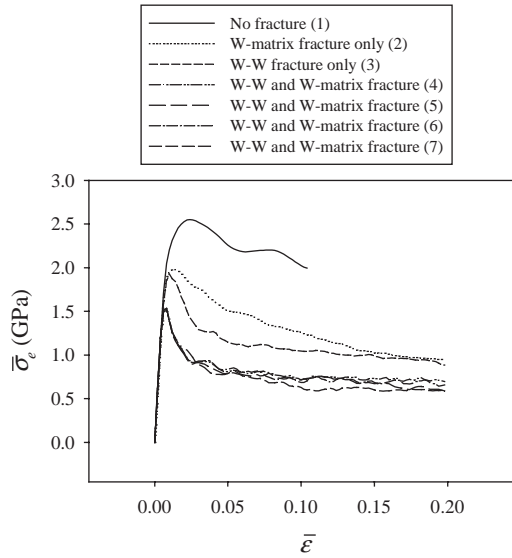


Fig. 16. Average effective stress, $\bar{\sigma}_e$, vs. applied axial stretch, $\bar{\epsilon}$.

that grain orientation and morphology only mildly influence the homogenized stress–strain behavior, lending us confidence that our sample of material is to a certain degree statistically representative with regards to effective mechanical stiffness, though more tests should be conducted to fully justify such an assertion. Weerasooriya (2003) performed quasi-static and higher rate Kolsky bar tension tests on WHA samples and measured the effective stress–strain response. At the highest rate conducted, $\dot{\bar{\epsilon}} = 750/\text{s}$, Weerasooriya (2003) predicted a peak uniaxial stress of 1.65 GPa (corresponding to $\bar{\sigma}_e = 1.35$ GPa) at a strain of $\bar{\epsilon} \approx 0.01$, followed by failure of the specimen by necking (i.e., tensile instability). Furthermore, peak stresses dropped and applied strains at peak stress increased as the applied strain rate was decreased in that series of experiments. It is difficult to compare the homogenized stress–strain behavior from our simulations to the macroscopic curves of those experiments (Weerasooriya, 2003) directly, since different sample sizes, strain rates, and boundary conditions were enforced in the experiments and simulations. However, the similarity in the range of peak stress values attained in experiment and simulation provide confidence in our selection of material parameters used to model plasticity and fracture. Notice also that the average effective stresses in the fracture simulations do not relax completely to a value of zero upon attainment of $\bar{\epsilon} = 0.20$. Values of the average stress $\bar{\sigma}_e$ are influenced by local stress concentrations near damage entities, residual stresses due to intergranular incompatibility, and out-of-plane and transverse stresses due to the imposed macroscopic boundary conditions. Fluctuations in stresses are also induced by inertial effects, though these are smoothed substantially by the averaging process. However, as will be shown later in Section 4.3, the average tensile stresses in the

direction of elongation do relax towards zero magnitude as a result of microcracking transverse to the loading direction.

Average temperatures $\bar{\theta}$ for the problem domain (i.e., for the entire FE mesh) are shown in Fig. 17, with $\bar{\theta} \equiv V^{-1} \int \theta dV$. The observed trend is a reduction in $\bar{\theta}$ with increasing occurrence of damage at interfaces, upon comparing values of $\bar{\theta}$ for cases 1–3 with those for cases 4–7 at particular time instances throughout the deformation history. This phenomenon is easily explained: microcracks in cases 4–7 accommodate much of the deformation accommodated by plastic strain in cases 1–3, leading to less cumulative plastic dissipation converted to heat in the former. Interestingly, for small magnitudes of applied stretch limited to $\bar{\epsilon} < 0.05$, rates of average temperature increase $\partial_{\bar{\epsilon}} \bar{\theta}$ in cases 2 and 3 exceed the rate of increase in the damage free case 1, as a result of extreme localized plastic deformation in the vicinity of damaged zones in cases 2 and 3. Such regions of extreme temperature rise (locally, $\theta > 1000$ K) are not observed in cases 4–7, as cracks can propagate more freely because fracture is active at both types of grain boundary interfaces, and fewer ligaments of localized plastic deformation and intense heating are formed.

Fig. 18 depicts the average fraction of plastic dissipation converted to temperature rise, $\bar{\beta} \equiv V^{-1} \int \beta dV$. Note that $0.9 < \bar{\beta} < 1.0$ throughout the duration of each simulation. Cases 1–3 achieve lower values of $\bar{\beta}$ throughout the deformation history than cases 4–7, since fracture suppresses plasticity and dislocation accumulation in the latter, especially in the W grains. Recall that the W grains comprise most of the volume of the sample (87.4%) and thus have the strongest influence on volume-averaged quantities such as $\bar{\beta}$. Rates of decrease $-\partial_{\bar{\epsilon}} \bar{\beta}$ for cases 2 and 3 exceed those for case 1 at low strain levels, again as a result of the emergence of ligaments of highly strained material in the vicinity of damaged zones where cracks are unable to

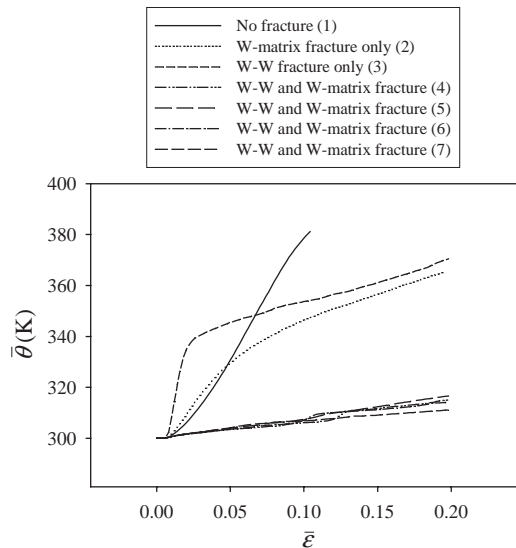


Fig. 17. Average temperature, $\bar{\theta}$, vs. applied axial stretch, $\bar{\epsilon}$.

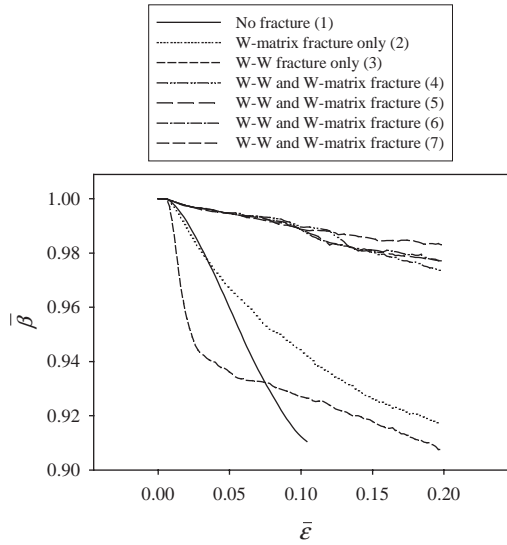


Fig. 18. Average dissipation fraction, $\bar{\beta}$, vs. applied axial stretch, $\bar{\epsilon}$.

propagate freely due to infinite cohesive strengths of one type of grain boundary interface.

4.3. Macroscopic damage modeling

An important objective of the present research effort is support of the construction of a physically realistic macroscopic model of the kinematics, thermodynamics, and kinetics of fully anisotropic damage for subsequent numerical implementation. Briefly addressing the kinematics of such a model, the net deformation gradient \mathbf{F} for a damaged material element containing k internal surfaces can be decomposed as (see derivation based on the generalized Gauss's theorem in Clayton and McDowell, 2003)

$$\mathbf{F} \equiv \underbrace{\frac{1}{V} \int_S \mathbf{x} \otimes \mathbf{N} dS}_{\text{external boundary}} = \underbrace{\frac{1}{V} \int_V \mathbf{f} dV}_{\text{average material deformation, } \bar{\mathbf{F}}} + \underbrace{\frac{1}{V} \sum_k \int_{S^{(k)}} \mathbf{x}^{(k)} \otimes \mathbf{N}^{(k)} dS^{(k)}}_{\text{internal surfaces (damage), } \mathbf{F}^d} = \bar{\mathbf{F}} + \mathbf{F}^d, \quad (47)$$

where S is the external surface of the volume element of referential volume V , with unit surface normal vector \mathbf{N} (referred to the reference configuration) and surface spatial coordinates \mathbf{x} . In Eq. (47), $\bar{\mathbf{F}}$ is the volume-averaged deformation gradient contribution from the intact material, and \mathbf{F}^d is the contribution from internal surface discontinuities associated with damage entities (e.g. cracks, voids, and shear bands), each with referential surface $S^{(k)}$, reference normal vector $\mathbf{N}^{(k)}$, and current coordinates $\mathbf{x}^{(k)}$. The premise of Eq. (47) for a polycrystal undergoing intergranular fracture is illustrated in Fig. 19.

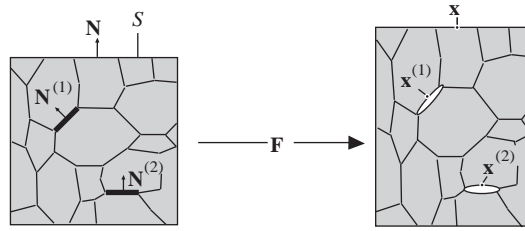
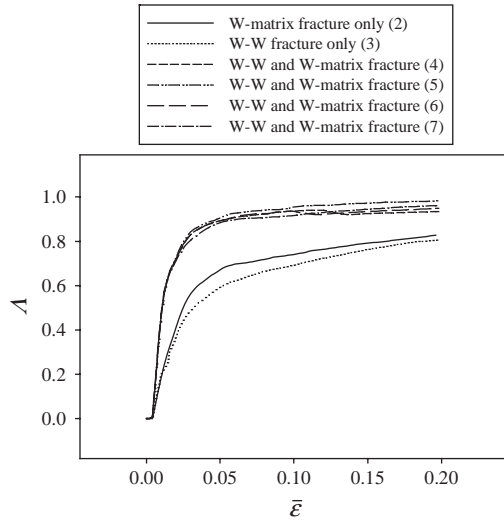


Fig. 19. Deformation and damage in a polycrystalline volume element.

Fig. 20. Damage accommodation, A , vs. applied axial stretch, $\bar{\epsilon}$.

Shown in Fig. 20 is a measure of the net accommodation of damage in the tensile direction, for the material volume elements (i.e., aggregates of W grains, matrix material, and cohesive fracture surfaces) in our numerical simulations 2–7, defined as

$$A \equiv \frac{F_{.2}^{d2}}{F_{.2}^2 - 1}. \quad (48)$$

Notice that at applied strains $\bar{\epsilon} > 0.06$, damage accommodates more than 90% (i.e., $A > 0.90$) of the total tensile stretch in cases 4–7, simulations in which cracks were permitted to open at W – W and W –matrix boundaries. In cases 2 and 3, in which fractures were restricted to W –matrix or W – W interfaces alone, respectively, damage accommodation is limited to a maximum of $A \lesssim 0.80$ at applied strains greater than $\bar{\epsilon} = 0.15$, still a considerably large fraction of the tensile component of the total prescribed deformation gradient \mathbf{F} .

Accompanying Eq. (47) is the definition of the net nominal stress tensor \mathbf{S} , work conjugate to the time rate of the net deformation gradient, $\dot{\mathbf{F}}$ (Clayton and McDowell, 2004):

$$\begin{aligned} \mathbf{S} \equiv & \underbrace{\frac{1}{V} \int_S \mathbf{X} \otimes \mathbf{t} dS}_{\text{traction carried by external boundary}} = \underbrace{\frac{1}{V} \int_V \mathbf{s} dV}_{\text{stress in material, } \bar{\mathbf{S}}} + \underbrace{\frac{1}{V} \sum_k \int_{S^{(k)}} \mathbf{X}^{(k)} \otimes \mathbf{t}^{(k)} dS^{(k)}}_{\text{traction carried by internal surfaces, } \mathbf{S}^d} \\ & + \underbrace{\frac{1}{V} \int_V \rho_0 \mathbf{X} \otimes (\ddot{\mathbf{x}} - \mathbf{b}) dV}_{\text{local inertia and body forces, } \mathbf{S}^i} = \bar{\mathbf{S}} + \mathbf{S}^d + \mathbf{S}^i, \end{aligned} \quad (49)$$

where $\mathbf{s} = \mathbf{j} \mathbf{f}^{-1} \boldsymbol{\sigma}$ is the local nominal stress in the material (transpose of the first Piola–Kirchhoff stress), \mathbf{t} is the traction vector per unit reference area along S , and $\mathbf{X}^{(k)}$ and $\mathbf{t}^{(k)}$ are reference surface coordinates and traction vector, respectively, supported by damage entity (i.e., cohesive surface) k . Shown in Fig. 21 is the average nominal stress component $\bar{S}^{22} = V^{-1} \int_V s^{22} dV$ for simulations 2–7, a variable which relaxes towards zero magnitude in each case as the applied deformation exceeds $\bar{\varepsilon} = 0.15$ and microcracking dominates the net elongation of the volume element. Comparing Figs. 20 and 21, we notice an inverse correlation between the volume-averaged nominal axial stress carried by the material, \bar{S}^{22} , and damage accommodation in the axial direction, A : generally, the greater the damage accommodation factor A , the greater the average load reduction in the aggregate as a result of distributed microcracking.

For direct comparison with the mode I-type damage observed in experiments (Weerasooriya, 2003) and in our numerical calculations, the following evolution

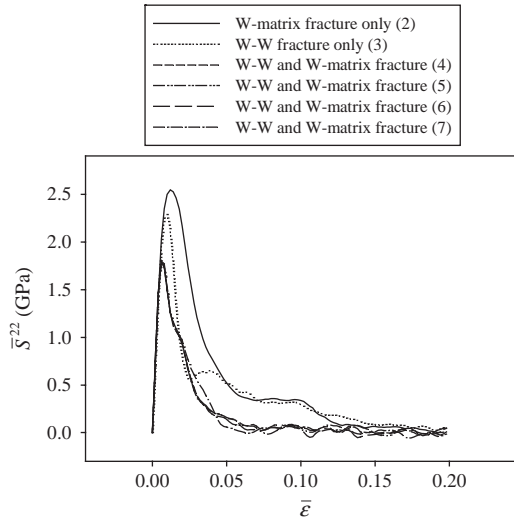


Fig. 21. Average axial stress, \bar{S}^{22} , vs. applied axial stretch, $\bar{\varepsilon}$.

equation is suggested below for diagonal components of \mathbf{F}^d :

$$(F^d)_{.A}^a = A \langle F_{.A}^a - \delta_{.A}^a \rangle, \quad \mathbf{F}_{t=0}^d = \mathbf{0}, \quad (a = A), \quad (50)$$

where the Macaulay brackets are necessary to ensure that mode I cracks do not contribute to compressive deformation of the volume element (i.e., no interpenetration of matter or negative crack opening displacements). Notice that Fig. 20 then provides the time history of A consistent with Eq. (50). For a given imposed total deformation gradient \mathbf{F} , the greater the magnitude of components of \mathbf{F}^d , the less strain accommodation by $\bar{\mathbf{F}}$, resulting in a reduction in magnitude of the average stresses carried by material, as is clear by comparing Figs. 16, 20, and 21.

Extending Eq. (50) to arbitrarily multi-axial deformations, we propose the following evolutionary description for the contribution of damage \mathbf{F}^d to the deformation gradient \mathbf{F} , assuming an undamaged, undeformed sample in the initial state:

$$(F^d)_{.A}^a = \hat{\Lambda}_{.b.A}^{a.B} (F_{.B}^b - \delta_{.B}^b), \quad \bar{\mathbf{F}}_{t=0} = \mathbf{1}, \quad \mathbf{F}_{t=0}^d = \mathbf{0}, \quad (51)$$

where $\hat{\Lambda}_{.b.A}^{a.B}$ is a stress-state dependent history variable of rank four—nonzero upon attainment of a critical nucleation criterion—scaling the degree of deformation accommodation from damage. Considering the effects of superposed rigid body motion in the spatial frame, $x^a \rightarrow Q_{.b}^a x^b + c^a$, with the unimodular matrix satisfying $\mathbf{Q}^{-1} = \mathbf{Q}^T$ and the spatially-constant translation vector c^a , we arrive at the following objectivity requirements:

$$\bar{F}_{.A}^a \rightarrow Q_{.b}^a \bar{F}_{.A}^b, \quad (F^d)_{.A}^a \rightarrow Q_{.b}^a (F^d)_{.A}^b, \quad \hat{\Lambda}_{.b.A}^{a.B} \rightarrow Q_{.c}^a Q_{.b}^{-1d} \hat{\Lambda}_{.d.A}^{c.B}. \quad (52)$$

Notice that Eq. (50) is a particular form of Eq. (52), where in Eq. (50) we have uncoupled components of evolution of damage deformation and total deformation corresponding to differing coordinate directions by letting $\hat{\Lambda}_{.b.B}^{a.A} \rightarrow A \delta_{.b}^a \delta_{.B}^A$. For complex imposed multi-axial deformations, relationships between components of the accommodation measure $\hat{\Lambda}_{.b.B}^{a.A}$ and average stress reduction in each spatial direction are expected, though specific forms of such relationships may not be trivially identifiable.

5. Conclusions

Constitutive models for constituents of a two-phase W–Ni–Fe tungsten heavy alloy have been developed within the framework of continuum crystal plasticity theory. The material models capture finite deformation, strain rate dependence, thermal expansion, thermal softening, heat conduction, and thermoelastic heating. Dislocation densities are treated as internal state variables that contribute to the strain hardening via a square-root dependency. Upon assuming a particular form for the residual free energy depending linearly upon the dislocation density, the framework allows computation of the stored energy of cold working. A cohesive zone approach has been used to model fracture at W–W and/or W-matrix interfaces

in dynamic finite element calculations simulating the tensile deformation of a polycrystalline aggregate of the heavy alloy.

Our numerical results highlight the following aspects of material behavior in the WHA system, within the context of high-rate ($\dot{\epsilon} = 10^4/\text{s}$) tensile simulations:

- W grains tend to support higher stresses than the matrix phase.
- Plastic strain, dislocation accumulation associated with cumulative strain hardening, and temperature rise due to plastic dissipation are generally much more pronounced in the ductile matrix phase than in the initially stiffer W grains.
- For a uniform magnitude of cohesive strength assigned to all interfaces, fracture tends to initiate at W–W grain boundaries rather than at W-matrix boundaries.
- Formation of macro-cracks of significant length (i.e., traversing the volume element) requires activation of fracture sites at both W–W and W-matrix boundaries.
- When interfacial fractures are simulated, cracks accommodate much of the deformation that would otherwise be accommodated by inelastic straining in the matrix phase, though regions of localized plastic flow and intense temperature rise frequently emerge in the immediate vicinity of damaged (i.e., cohesive) zones.
- Positive correlation exists between availability of fracture sites, net accommodation of deformation due to damage, and average stress reduction as a result of microcracking.

Our simulations have also shown that the macroscopic effective stress–strain behavior of the aggregate is only mildly influenced by the grain arrangement or the assignment of different random initial lattice orientations for either phase. However, it remains to be seen in future studies if prescription of a preferred set of grain orientations exerts a significant effect on the effective stiffness and the fracture behavior. Note that our conclusions are drawn in the context of 2D simulations; a fully three-dimensional finite element model of the composite polycrystalline microstructure, with cohesive fracture surfaces capable of tracking 3D crack propagation and interaction (Ortiz and Pandolfi, 1999), would be expected to represent some improvement in terms of capability of reproducing experimentally-observed fracture patterns.

Acknowledgements

S. Schoenfeld (ARL) is acknowledged for guidance and helpful discussion with regards to constitutive modeling and computational issues. T. Weerasooriya (ARL) and T. Bjerke (ARL) are thanked for providing optical images, experimental data, and modeling suggestions pertaining to material behavior. R. McGinty (Mercer University, USA) is acknowledged for contributing several algorithms used in the numerical simulations. Computations were conducted on U.S. Department of Defense high performance systems at ARL and ASC under resource allocation from Terminal Weapon Effects Project ARLAP01001600. Financial support of the

Weapons and Materials Research Directorate of the U.S. Army Research Laboratory is gratefully acknowledged.

References

- Aravas, N., Kim, K.S., Leckie, F.A., 1990. On the calculations of the stored energy of cold work. *J. Eng. Mat. Tech.* 112, 465–470.
- Argon, A.S., Maloof, S.R., 1966. Plastic deformation of tungsten single crystals at low temperatures. *Acta Metall.* 14, 1449–1462.
- Armstrong, P.J., Frederick, C.O., 1966. A mathematical representation of the multiaxial Bauschinger effect. CEEB Report No. RD/B/N, 731.
- Asaro, R.J., 1983. Crystal plasticity. *J. Appl. Mech.* 50, 921–934.
- Ashmawi, W.M., Zikry, M.A., 2003. Grain boundary effects and void porosity evolution. *Mech. Mater.* 35, 537–552.
- Bammann, D.J., 2001. A model of crystal plasticity containing a natural length scale. *Mat. Sci. Eng. A* 309–310, 406–410.
- Barenblatt, G.I., 1959. The formation of equilibrium cracks during brittle fracture: general ideas and hypotheses, axially symmetric cracks. *Appl. Math. Mech.* 23, 622–636.
- Belytschko, T., Chiapetta, R.L., Bartel, H.D., 1976. Efficient large scale non-linear transient analysis by finite elements. *Int. J. Numer. Meth. Eng.* 10, 579–596.
- Bjerke, T.W., Lambros, J., 2003. Theoretical development and experimental validation of a thermally dissipative cohesive zone model for dynamic fracture of amorphous polymers. *J. Mech. Phys. Solids* 51, 1147–1170.
- Boyer, H.E., Gall, T.L. (Eds.), 1985. *Metals Handbook*. ASM, Metals Park, Ohio.
- Bruchey, W.J., Herring, R.A., Kingman, P.W., Horwath, E.J., 1992. Deformation mechanisms in tungsten single crystals in ballistic impact experiments. In: Asfahni, R., et al. (Ed.), *High Strain Rate Behavior of Refractory Metals and Alloys*. TMS, Warrendale, PA.
- Bruchey, W.J., Horwath, E.J., Kingman, P.W., 1991. Orientation dependence of deformation and penetration behavior of tungsten single-crystal rods. In: Crowson, A., Chen, E. (Eds.), *Tungsten and Tungsten Alloys, Recent Advances*. TMS, Warrendale, PA.
- Cai, W.D., Li, Y., Dowding, R.J., Mohamed, F.A., Lavernia, E.J., 1995. A review of tungsten-based alloys as kinetic energy penetrator materials. *Rev. Particulate Mater.* 3, 71–132.
- Camacho, G.T., Ortiz, M., 1996. Computational modelling of impact damage in brittle materials. *Int. J. Solids Struct.* 33, 2899–2938.
- Clayton, J.D., McDowell, D.L., 2003. Finite polycrystalline elastoplasticity and damage: multiscale kinematics. *Int. J. Solids Struct.* 40, 5669–5688.
- Clayton, J.D., McDowell, D.L., 2004. Homogenized finite elastoplasticity and damage: theory and computations. *Mech. Mater.*, 36, 799–824.
- Clayton, J.D., Bammann, D.J., McDowell, D.L., 2004. Anholonomic configurations and metric tensors in finite elastoplasticity. *Int. J. Nonlinear Mech.* 39, 1039–1049.
- Coleman, B.D., Noll, W., 1963. The thermodynamics of elastic materials with heat conduction and viscosity. *Arch. Rat. Mech. Anal.* 13, 167–178.
- Costanzo, F., Walton, J.R., 2002. Steady growth of a crack with a rate and temperature sensitive cohesive zone. *J. Mech. Phys. Solids* 50, 1649–1679.
- Cuitiño, A., Ortiz, M., 1992. A material-independent method for extending stress update algorithms from small-strain plasticity to finite plasticity with multiplicative kinematics. *Eng. Comput.* 9, 437–452.
- Dandekar, D.P., Weisgerber, W.J., 1999. Shock response of a tungsten heavy alloy. *Int. J. Plasticity* 15, 1291–1309.
- Dugdale, S., 1960. Yielding of steel sheets containing slits. *J. Mech. Phys. Solids* 8, 100–104.
- Dümmer, T., Lasalvia, J.C., Ravichandran, G., Meyers, M.A., 1998. Effect of strain rate on plastic flow and failure in polycrystalline tungsten. *Acta Mater.* 46, 6267–6290.

- Espinoza, H.D., Zavattieri, P.D., 2003a. A grain level model for the study of failure initiation and evolution in polycrystalline brittle materials. Part I: Theory and numerical implementation. *Mech. Mater.* 35, 333–364.
- Espinoza, H.D., Zavattieri, P.D., 2003b. A grain level model for the study of failure initiation and evolution in polycrystalline brittle materials. Part II: numerical examples. *Mech. Mater.* 35, 365–394.
- Falk, M.L., Needleman, A., Rice, J.R., 2001. A critical evaluation of cohesive zone models of dynamic fracture. *J. Physique IV* 11, 43–50.
- German, R.M., Hanafee, J.E., Digiallonardo, S.L., 1984. Toughness variation with test temperature and cooling rate for liquid-phase sintered W-3.5Ni-1.5Fe. *Met. Trans. A* 15, 121–128.
- Gray, D.E., 1972. *American Institute of Physics Handbook*, third ed. McGraw-Hill, USA.
- Grüneisen, E., 1926. *Handbuch der Physik*. Vol. 10. Springer, Berlin, p. 1.
- Hill, R., 1963. Elastic properties of reinforced solids: some theoretical principles. *J. Mech. Phys. Solids* 11, 357–372.
- Hodowany, J., Ravichandran, G., Rosakis, A.J., Rosakis, P., 2000. Partition of plastic work into heat and stored energy in metals. *Exp. Mech.* 40, 113–123.
- Horstemeyer, M.F., McDowell, D.L., McGinty, R.D., 1999. Design of experiments for constitutive model selection: application to polycrystal elastoviscoplasticity. *Mod. Sim. Mat. Sci. Eng.* 7, 253–273.
- Horwath, E.J., 1994. The high strain rate deformation of tungsten single crystals. ARL-TR-620.
- Hutchinson, J.W., 1976. Bounds and self-consistent estimates for creep of polycrystalline materials. *Proc. R. Soc. Lond. A* 348, 101–127.
- Johnson, G.R., 1981. Dynamic analysis of a torsion test specimen including heat conduction and plastic flow. *J. Eng. Mat. Tech.* 103, 201–206.
- Johnson, G.R., Stryk, R.A., Holmquist, T.J., Beissel, S.R., 1997. Numerical algorithms in a Lagrangian hydrocode. WL-TR-1997-7039. Wright Laboratory, Armament Directorate, U.S.A. Approved for public release, unlimited distribution.
- Johnson, G.R., Stryk, R.A., Beissel, S.R., 2001. User instructions for the 2001 version of the EPIC code. Alliant Techsystems Inc., Hopkins, MN. Distribution authorized to U.S. government agencies and their contractors.
- Kallend, J.S., Huang, Y.C., 1984. Orientation dependence of stored energy of cold work in 50% cold rolled copper. *Metal Sci.* 18, 381–385.
- Kameda, T., Zikry, M.A., 1998. Three dimensional dislocation based crystalline constitutive formulation for ordered intermetallics. *Scr. Mater.* 38, 631–636.
- Kingman, P.W., 1997. Unique aspects of micromechanics in ballistic penetration. ARL-TR- 1412.
- Klopp, R.W., Clifton, R.J., Shawki, T.G., 1985. Pressure-shear impact and the dynamic viscoplastic response of metals. *Mech. Mater.* 4, 375–385.
- Kobytev, V.S., Lazareva, L.I., Popov, L.E., Pudan, L.Y., 1984. Build-up of strain defects and the energetics of plastic strain. *Izv. Vys. Uch. Zav., Fiz.* 4, 12–16.
- Kuhlmann-Wilsdorf, D., 1985. Theory of workhardening, 1934–1984. *Met. Trans.* 16A, 2091–2108.
- Kuhlmann-Wilsdorf, D., 1989. Theory of plastic deformation-properties of low energy dislocation structures. *Mat. Sci. Eng. A* 113, 1–41.
- Langer, S., Reid, A., Carter, C., Fuller, E., Roosen, A., 2003. PPM2OOF v1.1, website <http://www.ctcms.nist.gov/>.
- Lee, B.J., Vecchio, K.S., Ahzi, S., Schoenfeld, S., 1997. Modeling the mechanical behavior of tantalum. *Met. Mat. Trans. A* 28, 113–122.
- Lee, Y.J., Subhash, G., Ravichandran, G., 1999. Constitutive modeling of textured body-centered-cubic (bcc) polycrystals. *Int. J. Plasticity* 15, 625–645.
- Magness, L.S., 1994. High strain rate deformation behaviors of kinetic energy penetrator materials during ballistic impact. *Mech. Mater.* 17, 147–154.
- McGinty, R.D., 2001. Multiscale representation of polycrystalline inelasticity. Ph.D. Thesis, G.W.W. School of Mechanical Engineering, Georgia Institute of Technology.
- Needleman, A., 1987. A continuum model for void nucleation by inclusion debonding. *J. Appl. Mech.* 54, 525–531.

- Nix, W.D., Gao, H., 1998. Indentation size effects in crystalline materials: a law for strain gradient plasticity. *J. Mech. Phys. Solids* 46, 411–425.
- O'Donnell, R.G., Woodward, R.L., 2000. Influence of temperature on the fracture of a W–Ni–Fe alloy. *J. Mater. Sci.* 35, 4319–4324.
- Ortiz, M., Pandolfi, A., 1999. Finite-deformation irreversible cohesive elements for three-dimensional crack-propagation analysis. *Int. J. Num. Meth. Eng.* 44, 1267–1282.
- Qiu, X., Huang, Y., Nix, W.D., Hwang, K.C., Gao, H., 2001. Effect of intrinsic lattice resistance in strain gradient plasticity. *Acta Mater.* 49, 3949–3958.
- Ramesh, K.T., 1994. On the localization of shearing deformations in tungsten heavy alloys. *Mech. Mater.* 17, 165–173.
- Regueiro, R.A., Bammann, D.J., Marin, E.B., Garikipati, K., 2002. A nonlocal phenomenological anisotropic finite deformation plasticity model accounting for dislocation defects. *J. Eng. Mat. Tech.* 124, 380–387.
- Rice, J.R., 1968. Mathematical analysis in the mechanics of fracture. In: Lrebowitz, H. (Ed.), *Fracture, an advanced treatise*. Academic Press, New York, pp. 191–311.
- Rice, J.R., 1971. Inelastic constitutive relations for solids: an internal-variable theory and its application to metal plasticity. *J. Mech. Phys. Solids* 19, 433–455.
- Rice, J.R., Wang, J.-S., 1989. Embrittlement of interfaces by solute segregation. *Mat. Sci. Eng. A* 107, 23–40.
- Rosakis, P., Rosakis, A.J., Ravichandran, G., Hodowany, J., 2000. A thermodynamic internal variable model for the partition of plastic work into heat and stored energy in metals. *J. Mech. Phys. Solids*, 581–607.
- Scheidler, M., Wright, T.W., 2001. A continuum framework for finite viscoplasticity. *Int. J. Plasticity* 17, 1033–1085.
- Schoenfeld, S.E., Benson, D.J., 1997. Modeling penetration mechanisms and ballistic performance in high aspect ratio tungsten single-crystal rods: a crystal plasticity model suitable for impact calculations. In: Atluri, S.N., Yagawa, G. (Eds.), *Advances in Computational Engineering Science*. Tech Science Press, Forsyth, GA, pp. 1116–1121.
- Simo, J.C., Ortiz, M., 1985. A unified approach to finite deformation elastoplastic analysis based on the use of hyperelastic constitutive equations. *Comp. Meth. Appl. Mech. Eng.* 49, 221–245.
- Stevens, J.B., Batra, R.C., 1998. Adiabatic shear bands in the Taylor impact test for a WHA rod. *Int. J. Plasticity* 14, 841–854.
- Subhash, G., Lee, Y.J., Ravichandran, G., 1994a. Plastic deformation of CVD textured tungsten, part I: constitutive response. *Acta Metall. Mater.* 42, 319–330.
- Subhash, G., Lee, Y.J., Ravichandran, G., 1994b. Plastic deformation of CVD textured tungsten—II: characterization. *Acta Metall. Mater.* 42, 331–340.
- Svendsen, B., 2002. Continuum thermodynamic models for crystal plasticity including the effects of geometrically-necessary dislocations. *J. Mech. Phys. Solids* 50, 1297–1329.
- Taylor, G.I., 1934. The mechanism of plastic deformation of crystals. *Proc. R. Soc. Lond. A* 145, 362–415.
- Taylor, G.I., 1938. Plastic strain in metals. *J. Inst. Metals* 62, 307.
- Taylor, G.I., Quinney, H., 1934. The latent energy remaining in a metal after cold working. *Proc. R. Soc. Lond. A* 143, 307–326.
- Teodosiu, C., 1967. Contributions to the continuum theory of dislocations and initial stresses. I. *Rev. Roum. Sci. Techn. Méc. Appl.* 12, 961–977.
- Weerasooriya, T., 1998. Deformation behavior of 93W-5Ni-2Fe at different rates of compression loading and temperature. ARL-TR-1719, July 1998.
- Weerasooriya, T., 2003. Deformation and failure behavior of a tungsten heavy alloy under tensile loading at different strain rates. Presented at SEM Annual Conference on Experimental Mechanics, Charlotte, NC, USA, June 2–4.
- Weerasooriya, T., Beaulieu, P.A., 1993. Effects of strain rate on the deformation and failure behavior of 93W-5Ni-2Fe under shear loading. *Mat. Sci. Eng. A* 172, 71–78.
- Weerasooriya, T., Moy, P., Dowding, R., 1994. Effect of W–W contiguity on the high shear strain rate behavior of 93W-5Ni-2Fe tungsten heavy alloy. In: Bose, A., Dowding, R. (Eds.), *Proceedings of the*

- 2nd International Conference on Tungsten and Refractory Metals. Metal Powder Industries, pp. 401–409.
- Wei, Z., Yu, J., Hu, S., Li, Y., 2000. Influence of microstructure on adiabatic shear localization of pre-twisted tungsten heavy alloys. *Int. J. Impact Eng.* 24, 747–758.
- Wei, Z., Yu, J., Li, J., Hu, S., 2001. Influence of stress condition on adiabatic shear localization of tungsten heavy alloys. *Int. J. Impact Eng.* 26, 843–852.
- Woodward, R.L., O'Donnell, R.G., 2000. Tensile rupture of tungsten alloys by the cascade of crack nucleation events. *J. Mater. Sci.* 35, 4067–4072.
- Xu, X.-P., Needleman, A., 1994. Numerical simulations of fast crack growth in brittle solids. *J. Mech. Phys. Solids* 42, 1397–1434.
- Yadav, S., Repetto, E.A., Ravichandran, G., Ortiz, M., 2001. A computational study of the influence of thermal softening on ballistic penetration in metals. *Int. J. Impact Eng.* 25, 787–803.
- Yih, S.W.H., Wang, C.T., 1979. *Tungsten: Sources, Metallurgy, Properties, and Applications*. Plenum Press, New York.
- Zamora, K.M.O., Sevillano, J.G., Pérez, M.F., 1992. Fracture toughness of W heavy metal alloys. *Mat. Sci. Eng. A* 157, 151–160.
- Zhou, F., Molinari, J.F., 2004. Dynamic crack propagation with cohesive elements: a methodology to address mesh dependency. *Int. J. Num. Meth. Eng.* 59, 1–24.
- Zhou, M., 1993. Dynamic shear localization in a tungsten heavy alloy and ductile rupture in a spheroidized 1045 steel. Ph.D. Thesis, Division of Engineering, Brown University.
- Zhou, M., 1998a. Effects of microstructure on resistance to shear localization for a class of metal matrix composites. *Fatigue Fract. Eng. Mat. Struct.* 21, 425–438.
- Zhou, M., 1998b. The growth of shear bands in composite microstructures. *Int. J. Plasticity* 14, 733–754.
- Zhou, M., Clifton, R.J., 1997. Dynamic constitutive and failure behavior of a two-phase tungsten composite. *J. Appl. Mech.* 64, 487–494.
- Zhou, M., Clifton, R.J., Needleman, A., 1994. Finite element simulations of shear localization in plate impact. *J. Mech. Phys. Solids* 42, 423–458.
- Zikry, M.A., Kao, M., 1996. Inelastic microstructural failure mechanisms in crystalline materials with high angle grain boundaries. *J. Mech. Phys. Solids* 44, 1765–1798.

NO. OF
COPIES ORGANIZATION

1 DEFENSE TECHNICAL
(PDF INFORMATION CTR
ONLY) DTIC OCA
8725 JOHN J KINGMAN RD
STE 0944
FORT BELVOIR VA 22060-6218

1 US ARMY RSRCH DEV &
ENGRG CMD
SYSTEMS OF SYSTEMS
INTEGRATION
AMSRD SS T
6000 6TH ST STE 100
FORT BELVOIR VA 22060-5608

1 DIRECTOR
US ARMY RESEARCH LAB
IMNE ALC IMS
2800 POWDER MILL RD
ADELPHI MD 20783-1197

3 DIRECTOR
US ARMY RESEARCH LAB
AMSRD ARL CI OK TL
2800 POWDER MILL RD
ADELPHI MD 20783-1197

ABERDEEN PROVING GROUND

1 DIR USARL
AMSRD ARL CI OK TP (BLDG 4600)

NO. OF
COPIES ORGANIZATION

ABERDEEN PROVING GROUND

32 DIR USARL
AMSRD ARL CI HC
P CHUNG
AMSRD ARL WM
J MCCAULEY
T WRIGHT
AMSRD ARL WM MA
W NOTHWANG
AMSRD ARL WM TA
S SCHOENFELD
AMSRD ARL WM TC
M FERMEN COKER
R COATES
AMSRD ARL WM TD
S BILYK
T BJERKE
D CASEM
J CLAYTON (5 CPS)
T CLINE
D DANDEKAR
W EDMANSON
M GREENFIELD
C GUNNARSSON
Y HUANG
K IYER
R KRAFT
B LOVE
S MCNEILL
H MEYER
R MUDD
M RAFTENBERG
E RAPACKI
M SCHEIDLER
S SEGLETES
T WEERASOORIYA

INTENTIONALLY LEFT BLANK.